COMOTI
ROMANIAN RESEARCH & DEVELOPMENT INSTITUTE FOR GAS TURBINES

TURBO

Scientific Journal

vol. XI (2024), no. 1

2024 BSDA

Black Sea Defense & Aerospace EXHIBITION & CONFERENCE

9th Edition

Between May 22-24, 2024, the 9th edition of the exhibition of armaments and equipment intended for aviation and space took place in Romaero / Baneasa.

As part of the strategy to increase the institute's visibility, to strengthen existing relationships with partners in the field and to find new clients on these markets, COMOTI participated in this exhibition both with its own stand and with a joint stand, together with ARIE members - The Romanian Association of the Helicopter Industry.

The main activity took place at COMOTI stand where we were visited by both commercial representatives who wanted to find new customers to sell products and services, as well as by our important customers and potential collaborators.

During the opening ceremony, at the COMOTI booth, we received the visit of Romanian officials, including: the Prime Minister of Romania, Mr. Marcel Ciolacu, together with the President of the Romanian Senate, Mr. General Nicolae Ciuca, the Minister of National Defense, Mr. General Angel Tîlvăr, the Chief of Defense Staff, Mr. General Gheorghiță Vlad and the Secretary of State of the Minister of Research, Innovation and Digitization, Mr. Bogdan Mihai Dumea as well as representatives of the written and visual media.

At the COMOTI booth within ARIE, we received the visit of Mr. Daniel Davidi from IAI (Israel Aerospace Industries) having discussions related to a future collaboration to fulfill IAI's offset obligations resulting from the delivery to Romanian MoD of some satellite systems.

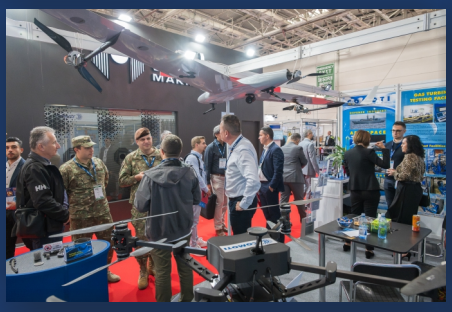

The presence of COMOTI at this event was a real success, strengthening relations with our current collaborators and partners in the industry, but also making COMOTI visible to potential clients.

Editorial Board

More information:
https://comoti.ro/turbo-scientific-journal-2/
jeni.vilag@comoti.ro

ISSN: 2559-608X

Scientific Journal TURBO is included in:
-ICI World of Journals:
ICV 2022: 61,82
ICV 2023: pending
https://journals.indexcopernicus.com/search/details?id=48512

-Directory of Open Access Scholarly Resources (ROAD)
https://portal.issn.org/resource/ISSN/2559-608X#

-Directory of Research Journals Indexing (DRJI):
http://olddrji.lbp.world/JournalProfile.aspx?jid=2559-608X

CONTENT

Editorial

Mai-binele (1)

În 1931 cartea *O sută de autori contra lui Einstein* [1] propunea o critică asupra teoriei relativității. Răspunsul acestuia: dacă *ar fi avut dreptate, era suficient unul singur.* Acesta este parte din farmecul publicațiilor științifice: faptul că o idee - oricât de obscură- odată publicată poate să detroneze convingeri dintre cele mai împietrite. Condiția este însă aceasta: să fie corectă; sau *"mai corectă"* decât ceea ce încearcă să înlocuiască.

Cu greu putem găsi o ramură literară în care apetitul pentru nou să fie mai mare decât în literatura științifică, nu atât în sensul de *inedit* cât de *revizuire*. Chiar dacă nu orice lucrare publicată poate fi *originală*, și poate nici nu ar fi util să căutăm cu orice preț originalitatea, majoritatea sunt *autentice* pentru că încearcă să răspundă unor întrebări reale într-un mod onest. Desigur, subiectivismul poate distorsiona percepția asupra propriei lucrări, mai ales când investiția personală este mare. Un etalon ar putea fi ca articolul pe care îl propunem să ne fi fost de folos atunci când am început cercetarea.

Când Montesquieu scria că *mai-binele este dușmanul de moarte al binelui* [2], nu a făcut doar un apel la acțiune - fie și imperfectă - ci și un avertisment că schimbarea, fie și în *mai-bine*, este inevitabil traumatizantă. Este mai puțin inutil acest *de moarte*, pentru că, dintre toate, ideile - prin natura lor greu coruptibilă - ajung să ne definească. Renunțarea la ele poate echivala cu dispariția unei părți din sine. Dar tocmai din acest motiv schimbarea poate fi asociată cu o renaștere [3] a însăși realității personale.

Este mai puțin evident, dar conceptele științifice - și cu atât mai mult articolele - sunt și ele perisabile. Este în egală măsură răsplata, dar și costul progresului.

Dacă așa stau lucrurile, atunci care mai poate fi rostul unei strădanii care - în cazul multora - reprezintă munca de o viață? Ce poate justifica un asemenea efort? Ce i-a putut impinge pe un Copernic sau pe un Galilei să își riște viața în căutarea unor răspunsuri pe care societatea lor nu doar că nu le cerea, ci le condamna chiar la nivelul de întrebare?

---

[1] Israel, Hans; Ruckhaber, Erich; Weinmann, Rudolf, eds. (1931). Hundert Autoren gegen Einstein. Leipzig: Voigtländer.

[2] Charles Louis de Secondat, Baron de La Brède et de Montesquie, Pensées 1726 - Le mieux est le mortel ennemi du bien -

[3] […] ce semeni nu dă viață, dacă nu va fi murit. (1 Corinteni 15:36)

Editorial

Mai binele (2)

În cele din urmă, fiecare dintre factorii motivaționali [4] va avea o pondere, în funcție de individ și de moment. Mi-ar plăcea să pot argumenta că ideologia este principalul factor în cadrul comunității științifice pentru că în spatele său aproape mereu stă căutarea adevărului. Dovada, însă, că răsplata materială domină *ecosistemul științific* o reprezintă însăși mecanismele prin care proliferarea publicării este încurajată și direcționată.

Scientometria [5] ca mecanism de control se folosește inevitabil de factori de impact, coeficienți și indici, toate menite să evidențieze și să încurajeze *calitatea*. Odată cu ea au apărut însă - tot inevitabil - și patologiile asociate, în special edituri de tip *vanity/predatory*, ori grupuri de autori care constituie adevarate *fabrici de articole*. Proporția în care acestea reușesc să vicieze actul științific depinde de măsura în care mediul academic și mai ales societatea ca ansamblu tolerează ca statisticile să devina scop în sine.

Relația fiduciară cu cititorul a fost dintotdeauna principalul pilon al calității comunicării științifice. Chiar dacă motivele din spatele publicării sunt diverse, totuși cel mai longeviv și cel mai dezinteresat (nu neapărat cel mai *sănătos*) rămâne cel ideologic.

E greu de crezut că scientometria va putea surprinde ceea ce în mod colectiv numim calitate, eliminând arbitrarul uman. Noi înșine, cititori, editori, autori, noi înșine suntem răspunzători de ceea ce producem și încurajăm. Nouă ne revine sarcina și privilegiul de a produce *mai-binele* sau măcar de a păstra sinceritatea procesului.

Iar ceea ce zic vouă, zic tuturor: Privegheați! (Marcu 13:37)

Dr. ing. Valeriu Drăgan

Iulie 2024

[4] Reward Ideology Coercion Ego; David L. Charney, M.D. and John A. Irvin, The Psychology of Espionage, Intelligencer: Journal of U.S. Intelligence Studies, 2016 p71

[5] Lingfei Wu, Aniket Kittur, Hyejin Youn, Staša Milojević, Erin Leahey, Stephen M. Fiore, Yong-Yeol Ahn, Metrics and mechanisms: Measuring the unmeasurable in the science of science, Journal of Informetrics, Volume 16, Issue 2, 2022, 101290, ISSN 1751-1577, https://doi.org/10.1016/j.joi.2022.101290.

Editorial

Le mieux (1)

In 1931 the book *One hundred authors against Einstein* [1] criticized the theory of relativity. Einstein's answer, If they were right, *one would have been enough*. This is part of the charm of scientific publishing: the fact that an idea, no matter how obscure, once out there can overthrow even the most hardened beliefs. The sole condition being that it is correct, or "*more correct*" than the one it tries to replace.

It is difficult to find a literary branch in which the appetite for new is greater than in science, not in the sense of *"novelty"* as much as *"revision"*. Although not every paper can be *"original",* and perhaps it would not be fruitful to seek originality at all costs, most papers are *"authentic"* because they seek to answer real research questions in an honest way. Of course, there will be a dose of subjectivism when viewing one's own work - particularly when the personal investment is significant. Still, a benchmark could be that the paper we submit would have been useful to us when we started the research.

When Montesquieu wrote "*Le mieux est le mortel ennemi du bien*" ("*Better is the mortal enemy of good*") [2], he did not just make a call to action - imperfect as it may be - but also issued a warning that change - *even for the better* - is inherently traumatizing. The word *"mortal"* is not without purpose, because ideas - by virtue of their incorruptible nature - end up defining us. Letting them go may - in some cases - equates to losing a part of self. Still, because of this, change can also be a chance for rebirth [3] of the personal reality.

It's not self-evident, but scientific concepts and papers are perishable, it is both the reward and cost of progress. If this is the case, what is the point of an effort that - in many cases - represents life's work? What could drive a Copernicus of Galileo to risk their very lives in the pursuit of answers to questions their society condemned.

[1] Israel, Hans; Ruckhaber, Erich; Weinmann, Rudolf, eds. (1931). Hundert Autoren gegen Einstein. Leipzig: Voigtländer.

[2] Charles Louis de Secondat, Baron de La Brède et de Montesquie, Pensées 1726 - Le mieux est le mortel ennemi du bien -

[3] […] what you sow does not come to life unless it dies. (1 Corinthians 15:36)

Editorial

Le mieux (2)

Ultimately, each of the motivational factors [4] will have its own weight, depending on the the individual and their current state. I would like nothing more than to argue that the main motivation in science is idealism, since it almost always implies the search for truth. However, the mechanisms by which research is encouraged and directed is evidence that material reward dominates the *scientific landscape*.

Scientometry [5] as a means of control inevitably makes use of indices, coefficients and impact factors, all meant to highlight and encourage *"quality"*. Alas, with it, pathologies such as *vanity/predatory* publishers or *paper milling* also are spawned. The percentage to which they manage to vitiate the act of science depends on the extent Academia - and society as a whole - allows statistics to become goals in of themselves.

The fiduciary relation with the reader has always constituted the foundation of proper scientific communication. Regardless of the reasons behind publication, the most disinterested (not necessarily the *soundest*) is idealism.

It is difficult to believe that scientometry will ever capture that which collectively we refer to as "quality", doing away with the human arbitrary. It is we, the readers, the editors, the authors, it is ourselves who bear the responsibility of what we produce and encourage. To us falls the task and privilege to bring forth this "*better*", or at least to keep the process honest.

"And what I say to you, I say to all: Watch!" (Mark 13:37)

Dr. Valeriu Drăgan

July 2024

[4] Reward Ideology Coercion Ego; David L. Charney, M.D. and John A. Irvin, The Psychology of Espionage, Intelligencer: Journal of U.S. Intelligence Studies, 2016 p71

[5] Lingfei Wu, Aniket Kittur, Hyejin Youn, Staša Milojević, Erin Leahey, Stephen M. Fiore, Yong-Yeol Ahn, Metrics and mechanisms: Measuring the unmeasurable in the science of science, Journal of Informetrics, Volume 16, Issue 2, 2022, 101290, ISSN 1751-1577, https://doi.org/10.1016/j.joi.2022.101290.

DAS DISTRIBUTED OPTO-ACOUSTIC SYSTEM IN REAL TIME WITH PARALLEL PROCESSING ON CUDA CORE

Andrei RADOI[1], Vasile PANGRATIE[1], Constantin PLOESTEANU[1], Andrei PANGRATIE[1]

Received: 12.12.2023
Accepted: 15.02.2024
Published: 18.07.2024
Corresponding author:
vpangrat@technovolt.ro.ro

ABSTRACT: Fiber optic detection uses the physical properties of light as it travels along a fiber to detect changes in temperature, deformation, and other parameters. Fiber optic detection uses the fiber as a sensor to create thousands of continuous sensor points along the length of the fiber. This is referred to as distributed fiber optic detection. Based on the technology of dynamic detection of optical fibers, a series of products have been introduced to the market, such as the detection of vibrations caused by intrusions into optical fibers, monitoring the security of the optical fiber line, and monitoring the security of optical fiber pipelines, with remarkable features. The aim of this paper is to present the results of a research project, conducted by Techno Volt's researchers, with the purpose of developing a measurement system based on fiber optic detection specialized in monitoring oil and pipelines.

KEYWORDS: DAS, monitoring, fiber optic detection, petrol, gas

1. INTRODUCTION

Until recently, manufacturers of pipeline leak detection devices and technologies employing distributed acoustic sensing (DAS) systems, have been using the interpretation of the acoustic signatures emitted by fluid escaping through cracks or gaps in pipelines. Interrogation is performed using the time-domain reflectometry (OTDR) technique and involves the scattering of Rayleigh, Brillouin, and Raman in optical fibers.
These leak detection techniques rely on the analysis of the acoustic "signatures" of events in pipelines and their differentiation from the normal situation ("footprint"). Using statistical algorithms, the analysis can generate errors and, consequently, false alarms, necessitating advanced frequency domain analysis techniques, determination of spectral and autocorrelation density for improving the signal-to-noise ratio, etc.

On the other hand, pipeline leaks introduce local temperature anomalies in the vicinity of the pipeline. Depending on the type of substance transported through the pipelines, the environment may experience local heating (for oil) or cooling (for gas pipelines). For the optimized transport of oil through pipelines, it is heated, and in case of leaks, the temperature around the ground increases, while leaks in pressurized gas pipelines introduce cooling due to gas expansion and the associated temperature decrease, through the so-called Joule-Thomson effect.

Consequently, monitoring the temperature around the pipeline can be an effective means of leak detection (DTS - Distributed Temperature Sensing systems). Usually, manufacturers use, as leak detection principles, monitoring temperature differences that occur around pipelines and their deformations due to accidental impacts or ground slips and collapses. Temperature detection techniques rely on the interpretation of Raman or Brillouin scattering signals. However, these technologies have limitations in detecting cracks (which require the detection of "acoustic fingerprints" in certain frequency domains).

[1] TECHNO VOLT SRL

Given these premises, our research team has developed INGRID, a monitoring system specialized in monitoring oil and gas pipelines with the help of fiber optics sensing technology, which we will further present.

2. DISTRIBUTED OPTO-ACOUSTIC SYSTEM

Following research in recent years, phase-sensitive time domain reflectometers -Φ-OTDR – have benefit of an important increase in performance. The applications in which they are used handle large amounts of data, resulting in the need to improve data processing by improving calculation algorithms and related hardware systems. Considering the continuously increasing computing power of GPUs, they have become a frequent choice in this field, in favor of classic solution based on CPU systems.
In [2], [3] and [4] are presented processing solutions which use parallel processing on GPU cores, but using classic optoelectronic schemes with simple amplitude detection.
In [5] and [7] are presented optical demodulation solutions with quadrature demodulator in order to reduce "fading" and to reduce also the processing requirements.
We combined the 2 solutions using a demodulation scheme with quadrature demodulator along with parallel processing with GPU cores, as described below.

INGRID is a distributed opto-acoustic system designed for monitoring the structural integrity of pipelines and the risks of intrusion in oil and gas transport networks. This system was developed through a partnership involving teams of specialists from UNST POLITEHNICA Bucharest, the Romanian Research and Development Institute for Gas Turbines – COMOTI Bucharest, and TECHNO VOLT SRL Bucharest.

The operation of the INGRID monitoring system is based on the principle of phase-sensitive time-domain reflectometry, where very short laser pulses are sent along an optical fiber and return reflected by the refractive index non-homogeneities within the optical fiber, through the phenomenon of Rayleigh scattering. The block diagram of the system is presented in the following figure:

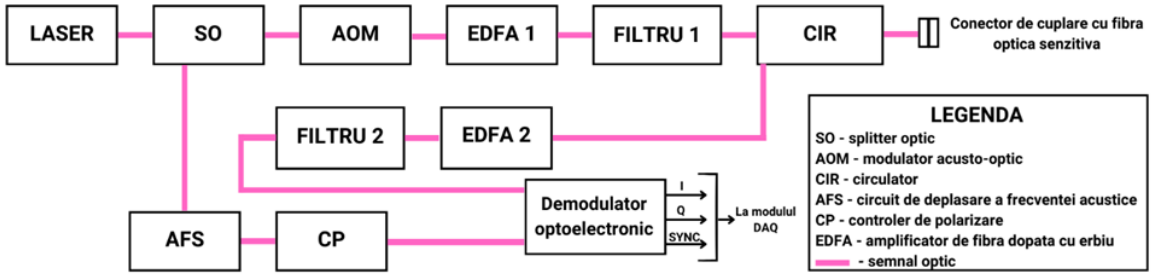

Figure 1. Block diagram of the INGRID system

An ultra-narrow bandwidth laser operating at 1550 nm is used as a light source with polarization-maintaining. The laser output is split into two branches by an optical splitter (SO) in a 10%:90% ratio. The 90% branch is modulated by an acousto-optic modulator (AOM) with a frequency shift of 200MHz to generate a very short optical pulse, where its duration directly influences the spatial resolution of event detection. The laser pulse repetition rate is on the order of kilohertz. The optical pulse is injected into the detection fiber through a circulator (CIR), and the reflected signal is applied to the quadrature hybrid demodulator. The 10% branch of the laser output is used as a local oscillator. An acoustic frequency shifter (AFS) circuit is employed to introduce a frequency shift equal to that of the acousto-optic modulator, ensuring that the reflected useful signal from the detection optical fiber and the local oscillator have the same frequency.

Before the optical signal from the local oscillator is injected into the hybrid demodulator, a polarization controller (CP) is inserted to align the polarization of the optical signal from the local oscillator with the selected polarization branch of the hybrid demodulator. The two quadrature outputs of the hybrid demodulator are then applied to an analog-to-digital conversion and processing system (DAQ) to extract useful information from the resulting electrical signal. The system also includes two Erbium-doped optical fiber amplifiers (EDFA) to compensate for losses and restore optimal levels of the optical signal, various filters to improve the signal-to-noise ratio, and connectivity elements.

To ensure real-time measurement, an optical demodulator of the useful signal and parallel processing of large-sized data blocks have been chosen. Thus, every second, data is processed along the entire length of the optical fiber. The optical demodulator is based on a 90° hybrid optical mixer that combines the Rayleigh

Backscattering (RBS) signal directly with the reference signal from the local oscillator (I component) and with the reference signal rotated by 90 degrees (Q component).

Assuming the backscattered signal from the optical fiber (RBS) can be described as:

$$A_S \cdot exp[i\omega_S t + i\varphi(t) + i\varphi_S] \tag{1}$$

where A_S,ω_S,φ_S represents the amplitude, angular frequency and initial phase of the signal, and φ(t) is the phase of the signal along the optical fiber, the electrical signals at the output of the demodulator are in the form:

$$\begin{cases} I_{AC} \approx \frac{1}{2} \cdot R \cdot A_S \cdot A_0 \cdot cos(\varphi(t) + \varphi_d) \\ Q_{AC} \approx \frac{1}{2} \cdot R \cdot A_S \cdot A_0 \cdot sin(\varphi(t) + \varphi_d) \end{cases} \tag{2}$$

The amplitude and phase of the signal can be obtained as follows:

$$\begin{cases} A_S \propto \sqrt{I_{AC}^2 + Q_{AC}^2} \\ \varphi(t) \approx arc\,tan\left(\frac{Q_{AC}}{I_{AC}}\right) - \varphi_d \end{cases} \tag{3}$$

The amplitude helps in positioning the event along the distributed optical fiber, and the phase is directly correlated with the signal induced in the fiber.

Characteristics of the system:

- Detection optical fiber length: 20km;
- Laser source wavelength: 1500nm;
- Laser pulse power transmitted into the fiber: 200mW;
- Pulse width: 50-100ns;
- Pulse repetition frequency: 8200Hz.

The data acquisition and processing system is based on the following components:

- Industrial PC with an i9 processor with 18 cores and 64GB RAM.
- NVIDIA RTX 4000 graphics card with 16GB GDDR6 memory on a 256-bit interface, a transfer rate of 448GB/s, 6144 CUDA cores, and 192 TENSOR cores, PCIe 4.0 interface.
- Data acquisition board with 2 channels and simultaneous acquisition, CompuScope, 16-bit resolution, data acquisition frequency of 500MS/S, and a frequency bandwidth of 350MHz.

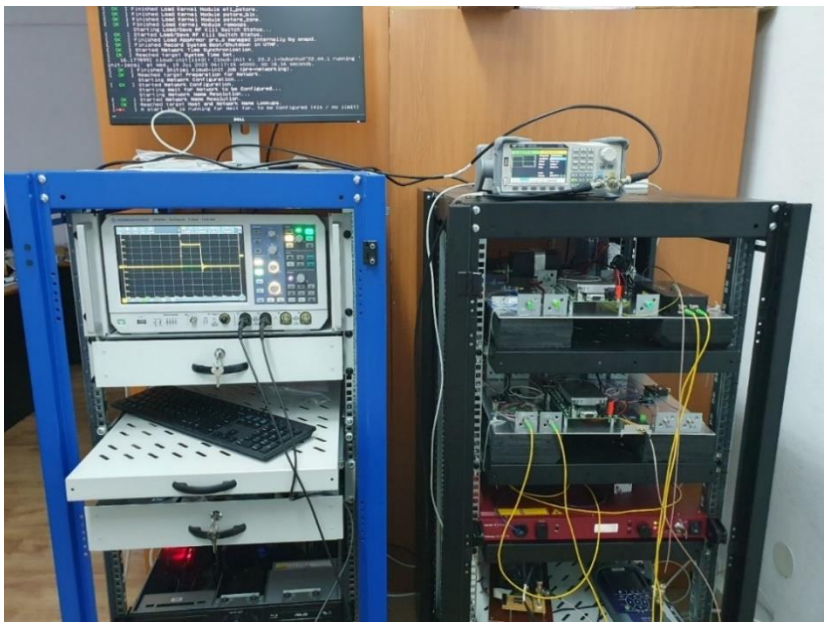

Figure 2. INGRID system

The acquisition program performs the data transfer from the CompuScope acquisition board to the GPU, carries out calculations on the GPU, synchronizes them with the CPU, and sends the results to the next analysis level. The CompuScope acquisition board has a sampling frequency set at 100MHz and is configured to read from two channels (I and Q) with 12256 samples from the moment of triggering. Each sample is 16 bits, and at the end of the acquisition, 128 octets representing the acquisition timestamp are appended.

At the end of the acquisition, a data segment of 49152 octets is obtained, consisting of data from the two channels and the timestamp. The segment is placed in the internal memory of the acquisition board in a circular "first in, last out" queue, from which the acquired information can be transferred to the CPU upon request into a compatible DMA buffer.

The program waits for 64 segments with each query sent to the acquisition board. Therefore, a compatible DMA buffer will have a size of 3145728 octets. In the program, 128 buffers of this size are allocated. Once all the data is received in a buffer, another thread takes over and begins transferring the data from this buffer to a buffer allocated on the graphics card (GPU). Thus, the segments from the CompuScope end up being placed in order in an initial GPU buffer. This buffer is 128 times larger than the buffers used between the CompuScope and the CPU, i.e., 402653184 bytes or 8192 segments.

Three initial buffers are allocated, and as soon as one buffer is filled with segments, the data translation operation is initiated—the first in a series of operations performed on the calculation thread, the third dedicated thread.

On the GPU, three buffers corresponding to the initial buffers are allocated, each storing two matrices, one for the I component and another for the Q component. Each component of the matrices is stored as a float in 4 bytes; the sizes of the two matrices are the same, i.e., 8192 columns (the number of segments in a calculation) and 12256 rows (the number of samples in a segment). Thus, the data from a row corresponds to a single sensor on the optical fiber. 1024 CUDA cores are used to arrange the data in this way.

By processing data from the two matrices, the amplitude $A = \sqrt{I^2+Q^2}$ and the phase $F = arctan\left(\frac{I}{Q}\right)$ of the signal received from the fiber are obtained. After completing the amplitude and phase calculation stage, the Fast Fourier Transform (FFT) calculation stage is initiated, where routines from the CUDA API are used to calculate in parallel one FFT for each of the 12256 rows of the previous matrices.

The results are saved in two other matrices, but this time with 4097 columns (source_size_FFT/2+1 or 8192/2+1) and 2 floats for each component, as the components now have both the real and imaginary parts. There are 3 such buffers, each with 803405312 bytes, one for each initial buffer.

The last transformation in the calculation stage is performed on the matrices containing the FFTs, where the top three highest values are retained from each row and stored in a new float buffer, with a size of 147072 octets. There are 3 such buffers, and 1024 CUDA cores are responsible for performing this transformation. At the end of the transformation, a significant filtering of the data that could be transmitted further or stored is achieved.

In total, there are 4 threads, of which 3 are dedicated:

- The thread that receives data from the CompuScope board.
- The thread that copies acquired data to the GPU.
- The thread that controls calculations on the GPU.

The last thread is the "main" thread, which generally handles communication with other programs, data transmission, and receiving external commands. This architecture was chosen to perform calculations simultaneously with data acquisition.

3. MEASUREMENT RESULTS

In the figure below, the following signals acquired and processed by the data acquisition system are presented:

- Raw signals acquired by the data acquisition board.
- I and Q signals at position 3000 from the distributed optical fiber sensor after the initial processing and storage in the corresponding matrices.
- FFT calculation results for the I and Q signals at position 3000.

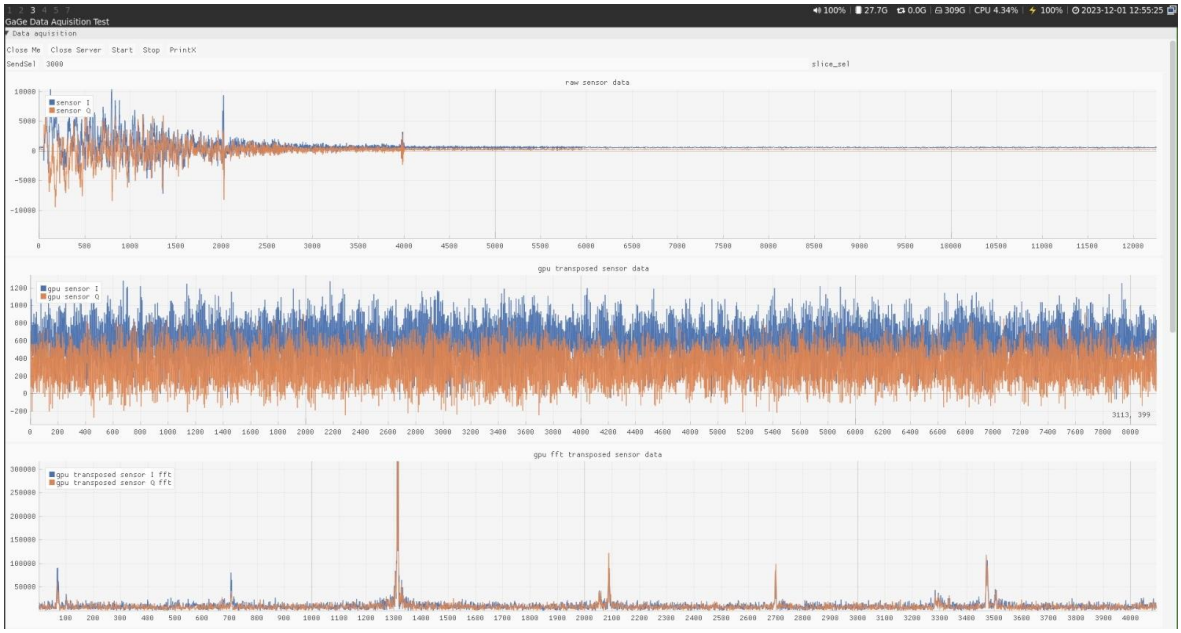

Figure 3. Measurement results of the fiber optic system

4. CONCLUSIONS

The optoelectronic demodulation scheme with a quadrature optical demodulator and parallel processing on the graphics card allows for the simultaneous measurement and analysis of optical signals originating from a distributed optical fiber sensor.

ACKNOWLEDGEMENT

The data presented and analyzed in this report were obtained with the help of COMOTI's Research and Experiments Center in the field of Acoustic and Vibrations staff and facilities.

The system referred to in this document - Distributed opto-acoustic system for monitoring the structural integrity of pipelines and the risks of intrusion in oil and gas transport networks – INGRID - is the result of a project financed within the Competitiveness Operational Program 2014-2020.

REFERENCES

[1] GPU-based acoustic feature extraction for electronic media processing – Conference paper, April 2011, Holger Blume, Leibniz Universitat Hanover

[2] Phase-sensitive optical time domain reflectometer with ultrafast data processing based on GPU parallel computation – Article, Vol. 57, No. 10 / 1 April 2018 / Applied Optics , Zhou Sha, Hao Feng, Yi Shi, Zhoumo Zeng, Tianjin University, China

[3] GPU-based fast processing for a distributed acoustic sensor using an LFM pulse – Article, Vol. 59, No. 35 / 10 December 2020 / Applied Optics, Shuanghao Wang, Junfeng Jiang, Shuang Wang, Zhe Ma, Tianhua Xu, Zhenyang Ding, Zhankun Lv, and Tiegen Liul, Tianjin University, China

[4] Co-Processing Parallel Computation for Distributed Optical Fiber Vibration Sensing – Article, Appl. Sci. 2020, 10, 1747; doi:10.3390/app10051747, YuWang, Yuejuan Lv, Baoquan Jin, Yuelin Xu, Yu Chen, Xin Liu and Qing Bai.

[5] Coherent Φ-OTDR based on I/Q demodulation and homodyne detection – Article, Optics Express · January 2016, Zinan Wang, Li Zhang, University of Electronic Science and Technology of China

[6] Optical Fiber Vibration Sensor Using Least Mean Square Error Algorithm – Article, Sensors 2020, 20, 2000; doi:10.3390/s20072000, Yu Wang, Jie Zou, Yuelin Xu, Yu Chen, Xin Liu, Qing Bai and Baoquan Jin, Taiyuan University of Technology, China
[7] Polarization Fading Elimination in PhaseExtracted OTDR for Distributed Fiber-Optic Vibration Sensing - Article WC4-2 OECC/PS2016, Guangyao Yang, Xinyu Fan, Bin Wang, Qingwen Liu and Zuyuan He State Key Laboratory of Advanced Optical Communication Systems and Networks, Shanghai Jiao Tong University, China
[8] Low Computational Cost Distributed Acoustic Sensing Using Analog I/Q Demodulation - Article, Sensors 2019, 19, 3753; doi:10.3390/s19173753, www.mdpi.com/journal/sensors, Fei Jiang, Zixiao Lu, Feida Cai, Honglang Li, Zhenhai Zhang, Yixin Zhang and Xuping Zhang

STUDY OF EMPIRICAL PERFORMANCE CALCULATION METHOD APPLIED FOR HIGH-LOAD MICRO AXIAL TURBINES

Bogdan-Cătălin NĂVLIGU[1], Răzvan-Edmond NICOARĂ[1], Alexandru HANK[1], Cosmin SUCIU[1], Dan GLASBERG[1] , Iulian VLĂDUCA[1]

Received: 16.01.2024
Accepted: 17.05.2024
Published: 18.07.2024
Corresponding author:
bogdan.navligu@comoti.ro

ABSTRACT: This manuscript delineates the significance of incorporating programmed tools in the turbine design process, introducing an algorithmic framework based on Ainley and Matheison's methodology. A comparative analysis is undertaken for the development of an axial micro turbine, aiming to elucidate the optimization potential of the algorithm when applied to turbines of reduced dimensions. In this context, the reference turbine and critical process components are detailed to provide comprehensive insights. Following the initial comparative simulation, a disparity of 56% on power field was identified, prompting an investigation into the error source. It was determined that the erroneous export of blade profile points resulted in a 3% increase in the minimum section. Subsequent modifications were implemented to rectify these discrepancies in accordance with established protocols.The study concludes by asserting the software's efficacy, demonstrating a maximum error of 5% in comparison to CFD simulations. This observed 5% discrepancy aligns with the broader discourse in the recent literature, wherein a 15% error range is acknowledged for current turbine blade designs. It is noteworthy that while the reference in this article stems from a CFD simulation, recent publications reference a real-tested engine as the basis for comparison.

KEYWORDS: Empirical Methods, Programmed tools, Axial Turbine, Micro-Turbine, High-Loaded Turbine

NOMENCLATURE

Yp - Profile loss coefficient
Ys - The coefficient of secondary flow losses
Yk - The coefficient of losses due to tip clearance
i - the angle of incidence of the gas flow at the vane entrance
i_s - the critical angle of incidence, defined as that angle at which profile loss is double compared to the case of zero incidence
f_6 – the function of profile loss with the incidence for typical turbine blading

1. INTRODUCTION

In the current state of the turbine design approaches it can be noticed that the main focus is put on the results corresponding to a nominal working regime, optimizing the calculations for a certain mass flow and

[1] Romanian Research and Development Institute for Gas Turbines COMOTI

rated speed. The primary procedures that warrant attention include the derivation of geometric, kinematic, and thermodynamic parameters specifically for the section at the mean radius. This involves incorporating the radius dimension to facilitate three-dimensional sizing. Subsequently, final adjustments are executed through numerical simulations. Furthermore, it can be noticed that a certain degree of difficulty exists because the calculations require a large number of iterations to obtain the desired turbine performance. In most cases, it is necessary to change the geometry and to reiterate the whole process several times, as every change of angle affects the change of velocity and hance the enthalpy drop. To address this challenge, a dedicated gas-dynamic calculation and blade profile computation program was formulated within the confines of the Romanian Research and Development Institute for Gas Turbine COMOTI, with a particular emphasis on its applicability to axial turbines. With the help of this developed program, the duration of the preliminary calculation can be optimized because the duration of iterations has been reduced. The methodology that imposes the calculation made by the program is in turn divided into several stages that deal with the main issues listed in the following [1].

Over time, several empirical methods have been developed for predicting the performance of axial turbines using the loss coefficients synthesized from experimental data obtained from a large number of turbines tested under the influence of different operating conditions[2-7] .

In the current state of the art related to the topic it can be noticed the focus on the reliabilty of correlations between the models assumed for losses and real data of turbine performances, studying how to enhance the range of practicability out of the design condtions established and how to improve the whole process. In this regard, Liu et al. has conducted a study where the emphasys was put on the statistical importance of correlations, being able to assemble a database from 109 cascades and achieving a relative error of total pressure within 15% in 50% of the cases [8]. This value of 15% can be met in other papers [9][10][11][12] as an acceptable value of deciding if the correlation can be considered accurate or not based on the reliabilty of the loss system.

Other improvements of empirical models such as the one by Aungier [13] offers an updated solution for more recent turbine configurations at the formulation of several important factors, with an advantage of multi-streamline analysis performance compared to the hypothesis of one-dimensional one that has been generally taken into consideration. This change leads to a better vadilation of the model for further 3D design stages bringing a more detailed representation of the fluid dynamics on the whole blade, from hub to shroud. It also brings up at the same time the importance of reliability in this stage of turbine configuration because the design parameters (which are the most influenced by this) that dictates further the three-dimensional processes of design. It can be noticed that Aungier based his study mainly on the Ainley and Mathieson model but also on the refinements made along the time by Dunham and Came [14] and Kacker and Okappu[15].

The latter ones have introduced the effect of exit boundary layer of trailing edges for axial entry nozzles and impulse blades in the losses caused at trailing edges[16], where is also considered (besides what is proposed in the Ainley and Mathieson model) the exit value of Mach, relevance of compresibility and Reynolds effects. Generally, the correlation produced by Ainley and Mathieson is considered to be the most fitting one because of three key-aspects. The first one relates to the mathematical aspect well established bringing more reliance than empirical associations. Secondly, the velocity distribution on the blade surface does not have to be assumed and the last one is that the system does not require any time-expensive computations for the implementation of calculus.

2. MATERIALS AND METHODS

2.1 Programing tool description

In order to verify the functionality of the program, in this paper will be used the following initial data as starting point in our hig-load microturbine design:

Table 1. Initial data

Massflow [kg/s]	Rotational speed [rpm]	Inlet Temperature [K]	Inlet pressure [Pa]	Power required [kW]
0.615	90000	1173	340558	95

The process is made up of a preliminary calculation, blade design, and the turbine characteristics which has to be done in many iterations, most of the time when an unsatisfactory solution appears, it is necessary to go back to the preliminary calculation

The third stage in the design of an axial gas turbine can also be completed by the determination of the operating behaviour of the turbine over the entire range of possible working regimes, respectively the determination of its operating characteristics. The algorithm presented, named „TCAR'' (Turbine Characteristic) can help to achieve an analysis of the turbine performance over different working regimes, as it will never function only under nominal conditions.

For the turbine characteristic to be obtained, the third-stage program needs a preliminary geometry. This preliminary geometry is the result of the initial turbine design data from the thermodynamic cycle and the velocity triangle. This process is done by two other subprograms first-stage program and second-stage program which are not discussed in detail in this article, but they constitute the preliminary calculation part for the last program. Figure 1 presents a comprehensive depiction of the operational workflow of the entire program. It is essential to emphasize that the input is human-derived, as opposed to being generated through a program loop—a selection made based on user`s experience with the program. For a detailed view of the blading designing program, there is an in-depth study of the whole process.[1]

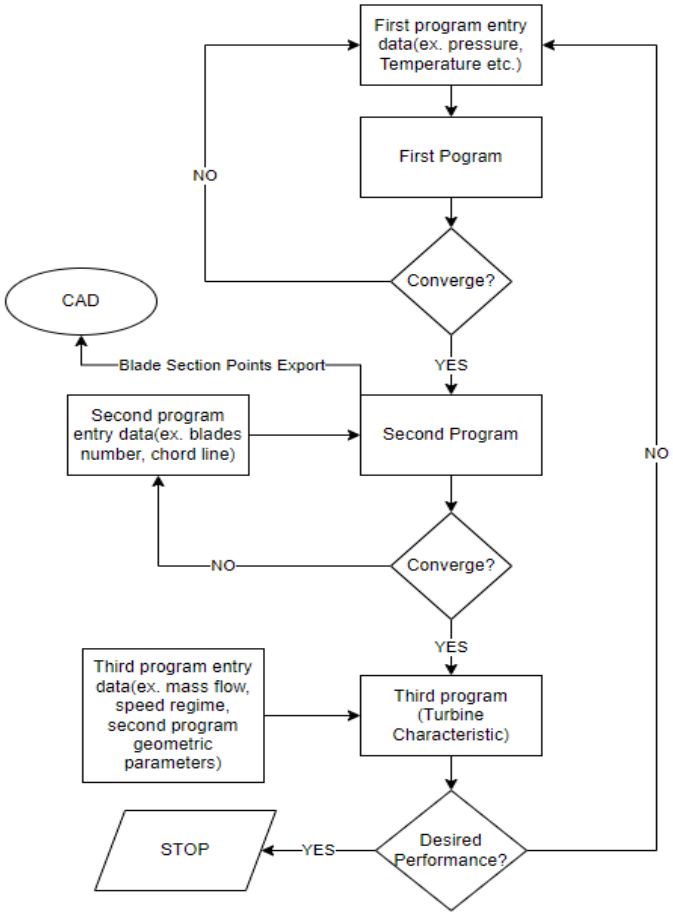

Figure 1. Workflow of turbine designing computation program

The input parameters of the third-stage program are the pressure and temperature at the entrance of the turbine stator, the nominal mass flow rate, the axial width of the stator and rotor, the number of rotor and stator blades, and the clearance at the tip of the rotor. In addition to these parameters, it is mandatory to know the geometry of the turbine stator and rotor blades, being necessary to identify the initial channel and define the flow through the turbine.

Regarding the TCAR program, it is not completely dependent on the first two programs. It can be used independently if the stator and rotor geometry together with the input parameters are known to us.

The preliminary calculation implies a series of input parameters:

- Radius at the entrance of the turbine stator for each design section.
- Radius at the turbine exit for each design section.
- The flow angle of each turbine component entrance, in relative motion for the rotor (absolute for stator).
- The flow angle of each turbine component exit, in relative motion for the rotor (absolute for stator).

- The Mach number at the exit of each turbine component, in relative motion for the rotor (absolute for stator).

The geometric parameters must be known for a number of minimum three sections(hub, tip, and median radius) of the stator and rotor blade. In this study eleven sections were consider enough for a precise geometry. These parameters are:

- Calculation radius [m];
- Minimum opening [m];
- Chord length [m];
- Maximum thickness [% of the chord length];
- Leading edge angle of the profiles
- Trailing edge radius.

Ainley and Mathieson's method [2] is used to determine the gas flow angle at a turbine component exit. This method considers the flow through each stage only at a single reference radius. However, this method will also be used in three-dimensional calculations, assuming that at any radius the gas angle depends only on the parameters corresponding to that radius. Ainley and Mathieson's method [2] take into consideration that the geometry of the vanes and the Mach number at the exit of the turbine are the main factors that influence the methodology. Regarding the angle of the gas flow at the exit of each turbine component the method assumes that the gas flow is independent of the inlet angle.

The program systematically resolves velocity triangles and subsequently integrates considerations for losses through the utilization of empirically derived formulas, which are established based on experimental results from testing a considerable number of axial gas turbines**.** The subsequent subchapter will provide a more in-depth discussion of the topic. Upon successfully completing the workflow outlined in Figure 1 and achieving a satisfactory outcome, the construction of a 3D model becomes feasible.

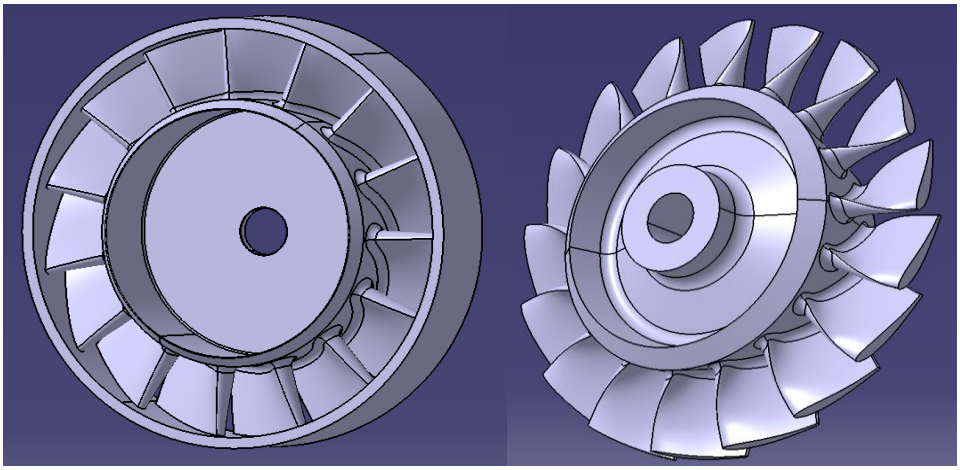

Figure 2. The 3D model for stator and rotor

Table 2. 3D geometrical aspects

	Vane	**Rotor**
Blade number	15	17
Shroud radius [mm]	52	52
Hub radius [mm]	34	26
Tip clearance [mm]		0.25

2.2 The Loss Coefficients System, Thermodynamic parameters and calculation method

Ainley and Mathieson's method [2] says that a total pressure loss coefficient in a turbine component of axial vanes is the sum of profile , secondary and tip clearance loss coeficients witch are corelated with the pressure as it follows:

$$Y_T = Y_P + Y_s + Y_k = \frac{P_1^* - P_2^*}{P_2^* - P_2} \quad (1)$$

The calculation of the pressure loss coefficient at a certain radius of the vane of each turbine component is made on the assumption that this coefficient depends only on the characteristics found at that radius. However, this hypothesis is not entirely realistic, because secondary losses and losses due to tip clearance are not equally distributed along the radius, but their variation regarding this aspect does not have such an influential impact on the results to consider that this hypothesis cannot be applied for this approximation of losses [2].

Another assumption in the determination of the loss coefficients according to the method of Ainley and Mathieson is that they are not influenced by the Mach number of the gas flow. From this perspective, it is unlikely that this method will lead to considerable errors unless the resulting vanes have a high degree of curvature of the upper surface in the vicinity of the trailing edge.

Another important aspect consists of the system of reference of the flow relative to the blades of each turbine component. Thus, the relative flow parameters are used to describe the rotor and in the case of the stator, absolute parameters are applied.

The determination of the thermos-gas dynamic parameters and the similitude parameters, necessary for drawing the characteristics of an axial gas turbine, for which the geometry is known, is done by solving the fundamental equations of the flow in the selected sections for calculation between the vane of each turbine component, for each possible working regime of the turbine. This calculation method requires the definition of the following groups of parameters:

- The geometric parameters, which define the shape of the flow channel and the profiles of the vanes.
- Thermogasodynamic parameters are considered known for all operating regimes.
- The parameters that define the operating mode of the turbine (gas flow rate, total temperature, and total pressure in the turbine inlet section and speed).

The flow parameters are determined successively for each calculation section, starting with the turbine inlet section, by the following points:

- Solving the energy equation for each streamline
- Solving the equation of motion along the height of the flow channel
- Checks the continuity for the entire flow channel and each current tube.

Since it is not possible to solve the equations that govern the flow straight-forward analytically speaking, an iterative calculation method is used. At first, the solutions are found without considering the influence of the slope and the curvature of the streamlines. The radial displacements of the streamlines, resulting from the first iteration, are then used for the next iteration.

All the derived forms of the variables used in the program are calculated with the help of the finite difference method. The calculation program determines the flow conditions along 5 streamlines. The flow from the turbine inlet section is considered uniform so that the radii of the streamlines, which divide the gas flow into equal parts, and the thermos-gas dynamic parameters corresponding to each streamline can be easily calculated.

For the exit section from the stator, the position of the streamlines and the magnitude of the axial velocity at the median streamline are established in the first approximation. Considering the constant axial velocity along every section, the gas discharge angles and the loss coefficients for each streamline are determined in the first approximation. Knowing these quantities, the equation that describes the motion can be solved through iteration. In essence, this equation can be reduced to the form [17]:

$$\frac{d(\ln Y^2)}{dx} = I(x) \tag{2}$$

By integrating this equation using as ends of integration the boundary condition (x=1 and y=1) will be obtained:

$$\ln Y^2 = \int_1^x I(x) \cdot dx \tag{3}$$

And

$$Y = e^{\frac{1}{2}\int_1^x I(x)\cdot dx} \tag{4}$$

The solution of this equation is found by the method of sequential approximations, assuming approximate values for Y(x) and checking the equation. After solving the equation, all the flow conditions in the exit section from the stator are known and the total continuity equation can be solved [18].

$$Y_p = Y_{p(i=0)} \cdot f_6\left(\frac{i}{i_s}\right) \tag{5}$$

Similarly, this iterative method is also applied to the following calculation sections. Finally, the program calculates the similitude parameters for tracing the turbine's operating characteristics.

2.3 CFD Simulations Approach

From the presented 3D geometry of the microturbine, the stator blade and rotor blade domain has to be extracted for simplicity in order to verify the results obtained with „TCAR'' program with CFD simulation. A visualization of the reference turbine domain that was designed using the three-stage program is shown below, the same turbine domain used in this paper for numeric simulations:

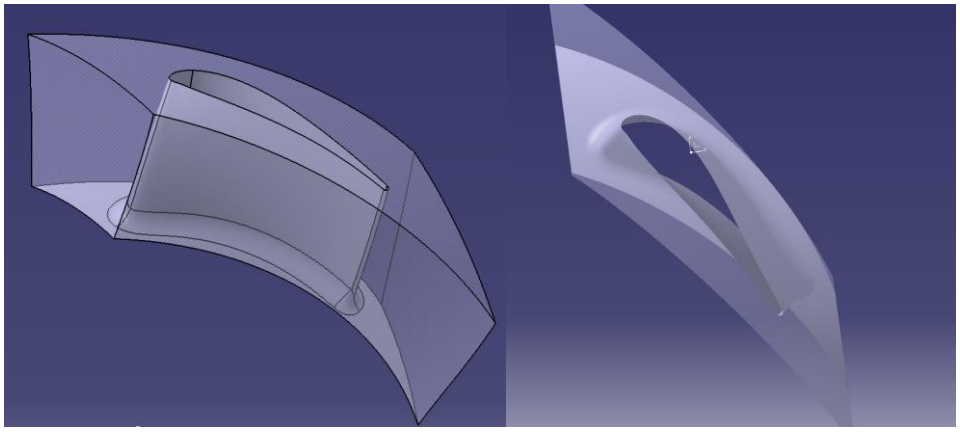

Figure 3. Stator blade domain

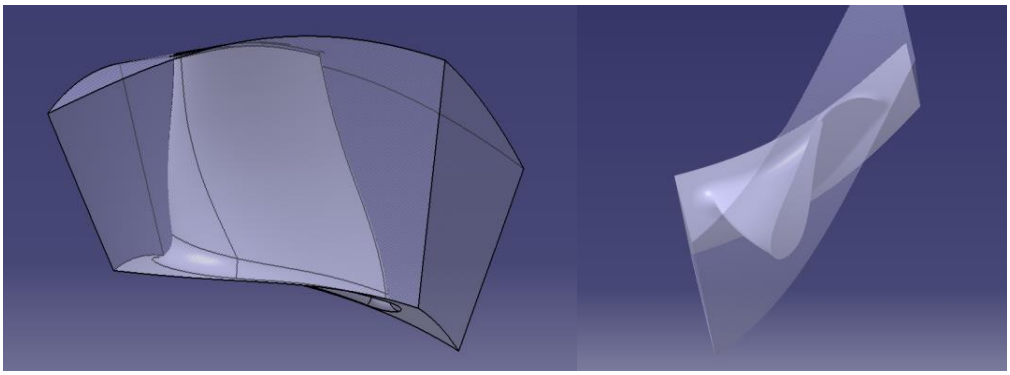

Figure 4. Rotor blade domain

For further numerical simulation, the Ansys CFX software was used with the following mentions: boundary conditions are pressure and temperature on the vane inlet and mass flow at rotor exit, turbo mode was used to set up the solver, match control was used in both stator and rotor mesh for the periodic sides of the domain and a 10 layer inflation was used between the blade and the domain. For all simulations, air ideal gas was used as the working fluid. The mesh is unstructured and was generated using Ansys Mesh, Figure 5 presents the resulting mesh for both the vane and rotor. In the case of turbines, the flow does not exhibit an adverse pressure gradient; therefore, an unstructured grid suffices. The number of elements and nodes for both parts are presented in Table 3. It has to be mentioned that an interface between the vane and rotor has been created and the rotor domain`s shroud was set as Counter Rotating Wall.

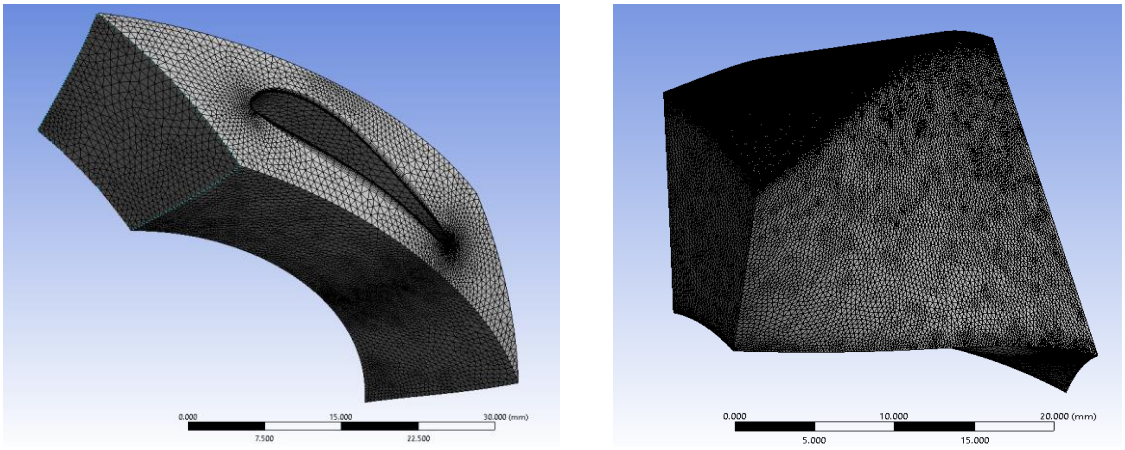

Figure 5. Mesh grid for stator domain and rotor domain

Table 3. Mesh grid elements and nodes

Domain	elements	nodes
rotor	1562251	370190
stator	634404	160206

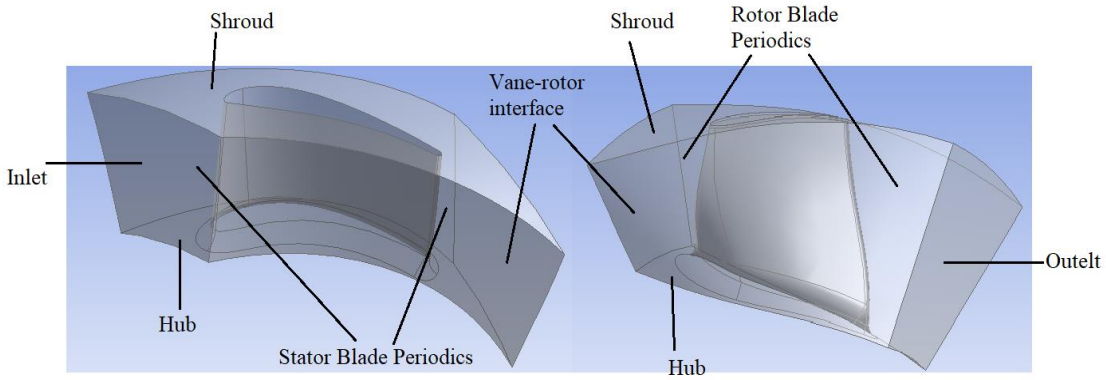

Figure 6. Numerical domains and boundary conditions

Table 4. CFD boundary conditions

Boundary condition location	condition
vane domain`s inlet	temperature=1123[K] pressure= 340558 [Pa]
rotor domain`s outlet	mass flow= 0.615 [ks/s]
rotor domain`s shroud	CounterRotating Wall

After running the computer simulations for fluid dynamics, the accuracy of the results will be verified by examining a parameter called the Yplus number. The distribution of this number across the system is illustrated in the image below.

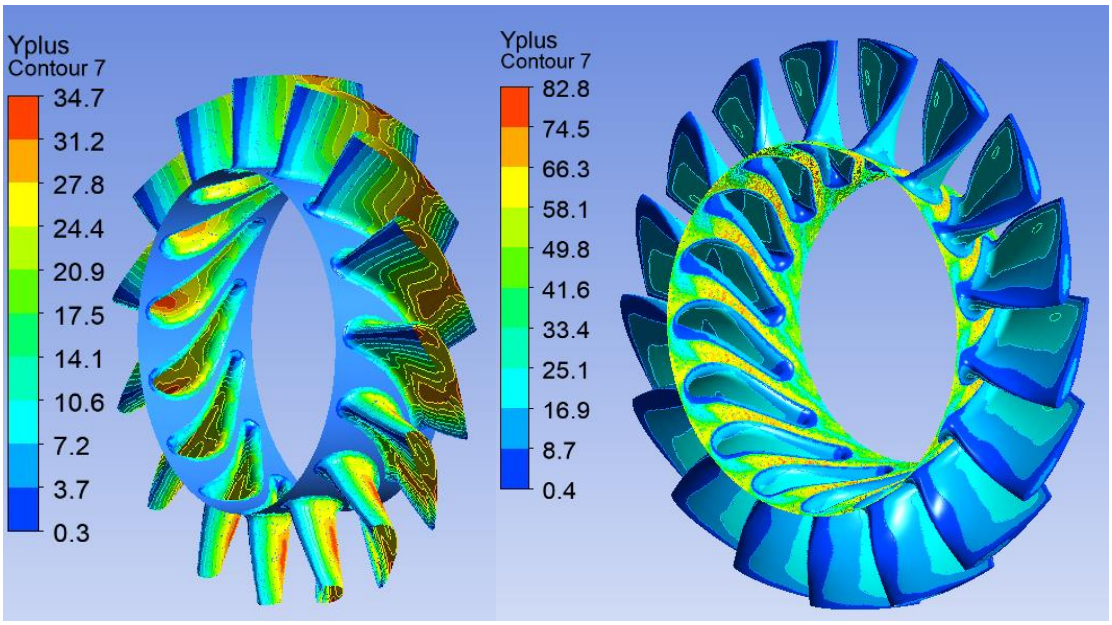

Figure 7. Yplus for vane and rotor geometry

Observations reveal that, for the selected turbulence model (K-Epsilon), the Yplus number remains within the range of 100. This observation suggests that the impact of the mesh on the obtained results is minimal.

3. COMPARISON BETWEEN TCAR AND CFD METHODS

Typical aircraft engine turbine performance usually fell within ± 3 percent of the original predictions, but much larger errors occurred with certain unusual designs and with small turbines.[14]It can be once agin higlited the current literature with its 15% error claim for modern turbine blade designs. Therefore, in this paper a study is conducted to test the ultimate limits of the third-stage program developed by the Romanian Research and Development Institute for Gas Turbines COMOTI using Ainley and Mathieson's method, thus a microturbine with as much torsion as possible was selected.

After conduncting the first CFD simulation a comparison between the two methods have been described by the table below. It was observed that there is a 56% diference on power field witch conducted to an investigation of numerical and geometrical parameters for errors.

Table 5. Output parameters

	TCAR program results	**CFD results withoud CAD scaling**
P2 [Pa]	181754	274279
T2 [K]	1032	1105
Isentropic efficiency [%]	83.71	90.33
Power [kW]	95	42

It was found during the use of the calculation program that it requires a modification on the radii at the base and the top in the stator and rotor domains to obtain a similar characteristic in the simulation of the 3D geometry of the entire turbine. The cause of this requirement is the result of exporting the 2D section points in a CAD (Computer Aided Design) program. The exported points generate a larger minimum section than the reference minimum section used by the third-stage program in its calculation.

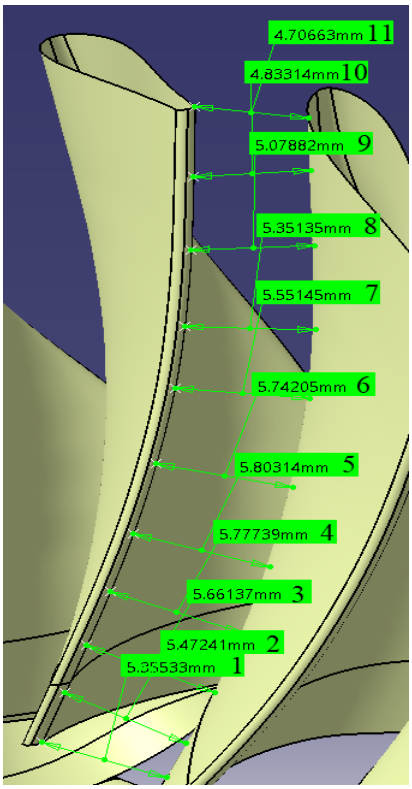

Figure 8. Minimum distance for each radius after building blades with exported points from the second-stage program

Table 6. Minimum distances for every 11 sections generated by the program

sections	Program minimum sections [mm]	Exported sections minimum distance [mm]
1	0.005362	0.0053533
2	0.005412	0.00547241
3	0.00541	0.00566137
4	0.005374	0.00577739
5	0.005314	0.0058031
6	0.005227	0.00574205
7	0.005117	0.00555145
8	0.004986	0.00535135
9	0.004838	0.00507882
10	0.00468	0.00483314
11	0.004514	0.00470663

As shown in Figure 8 and Table 6 there is a minor difference between the program minimum section and the CAD minimum section. This difference between the two minimum sections is the result of the Ainley and Mathieson method residuum due to the fact that the calculation is done for a 2D streamline section where was added a correction based on a coefficient specific for this method to generate a stream tube (domain of the flow) from which the mass flow is desired to be obtained.

For various turbines designed with this program and its calculation method, it was observed that this correction needs to be adjusted by 2-4% regarding the appreciation of the tube to avoid further modifications of the domain.

The adjustment of this correction coefficient is necessary because the total parameters resulting from the numerical simulations without modifying the channel have a higher value following the isentropic expansion carried out when passing through the turbines than those resulting from the calculation method used by the program developed by the RomanianNational Research and Development Institute for Gas Turbines Comoti, as it is necessary to achieve a certain acceleration of the fluid to generate a greater pressure drop and implicitly a greater power.

Minimum scaling iterations upon the CAD were made to obtain the desired domain. Thus, a resemblance was observed between the numerical simulation results carried out for the nominal case and the third-stage program results.

Table 7. Output parameter after scaling

	TCAR program results	CFD results with 3% CAD scaling
P2 [Pa]	181764	191301
T2 [K]	1034	1013
Isentropic efficiency [%]	83.71	87.81
Power [kW]	94	98.6

From the analysis of the resulting parameters obtained by the two methods,it can be highlighted in Table 7 that the calculation realized on the nominal regime (90 000rpm and 0.615 kg/s) by the computing program is accurate. The difference between computational program and CFD isentropic efficiency is an effect of the method itself and the severe choice of coefficients. Further simulations studying multiple operating cases of the turbine will be made to verify the functionality of the program developed within the Romanian Research and Development Institute for Gas Turbines COMOTI.

By definition, the universal characteristic of an axial turbine represents a set of curves that contain variations of the gas expansion ratio concerning the similarity parameters of mass flow rate and rotational speed [19]. In the next graph, calculations have been made using the third-stage program for multiple values of the mass flow and rotational speed. In the same manner, parametrical set CFD software has been used to vary the rotational speed and mass flow to obtain the performance of the respective turbine and to generate the turbine characteristics. The chart lines representing the reduced mass flow ($m_{red} = (m\sqrt{T})/p$ [kg/s * √K /Kpa]).

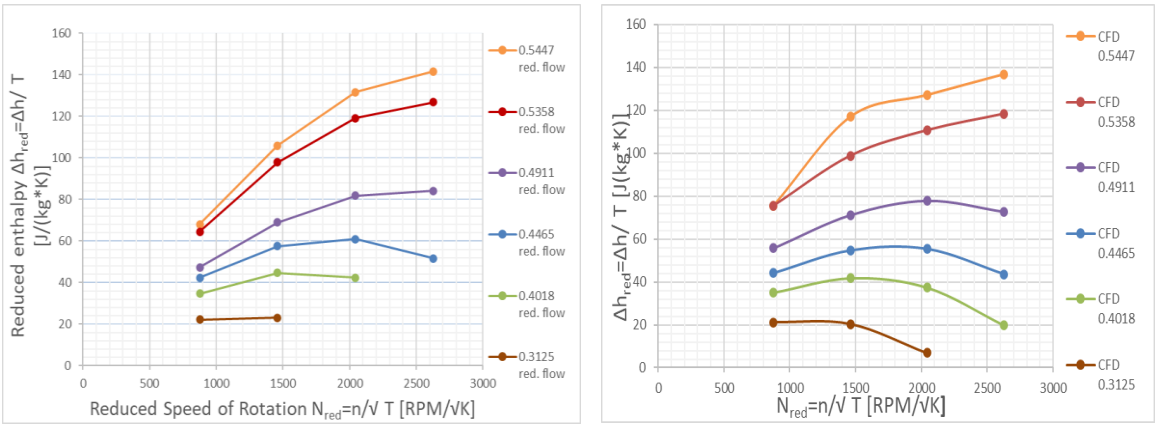

a) b)

Figure 9. A) „TCAR" Turbine Characteristics B) CFD Turbine Characteristics

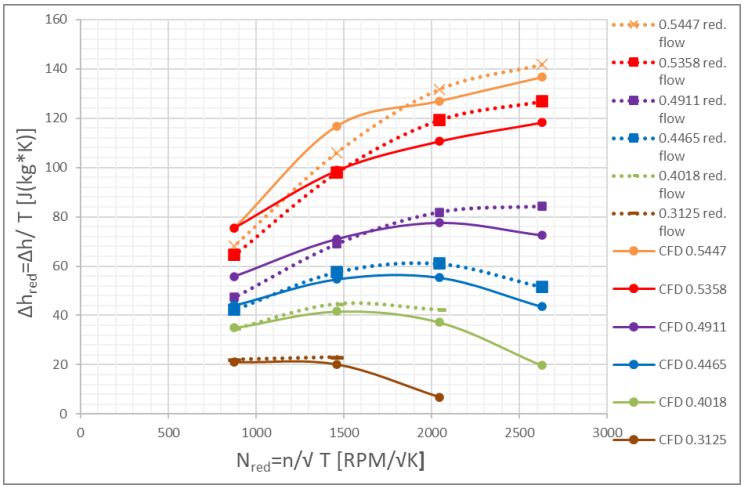

Figure 10. The overlaid maps of the universal turbine characteristic for CFD and „TCAR"

As shown in Figure 9 and Figure 10 there are minor differences between the calculation results using the third-stage program and the CFD simulation results for the same turbine, these differences occur as a sum of multiple neglectable differences between the methods such as losses coefficients and the appreciation coefficient of the current tube from the current line caused by the extremely torsion of the rotor blade that has been chosen for this paper. All these differences tend to have greater value in this particular case of a high-loaded microturbine than in the process of designing a usual axial turbine.

Despite these errors caused by the design of a turbine at the limit of the method, the outcome of the turbine characteristics is similar and is acknowledged the functionality of „TCAR'' program, the difference being in the 2-5% range with a greater difference for lower speed regimes and lower mass flow value, for example:

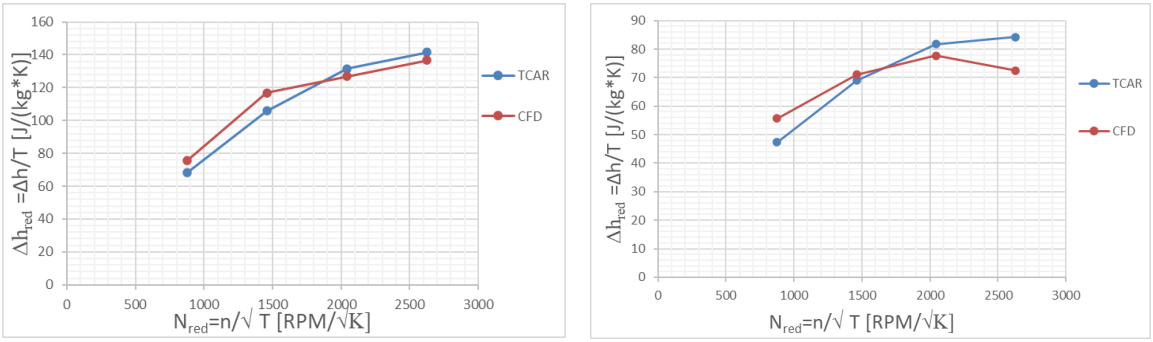

a) **b)**

Figure 11. „TCAR"-CFD comparison forA) nominal flow and B) 0.55 kg/s mass flow

4. CONCLUSIONS AND FUTURE WORK

This paper has proven the functionality and value of the programmed tool based on the Ainley and Mathieson empirical method for turbine characteristics calculation developed by the Romanian Research and Development Institute for Gas Turbines COMOTI by providing similar results as CFD simulations. Time was an important factor in this process since a minimum number of iterations with this particular method were needed to design a specific microturbine, while traditional methods would lead to many more iterations of CFD simulations, whose duration is exponentially longer, and additional modifications of the blading design.

The marginal difference of 2-5% observed between the discussed method and the CFD simulation warrants consideration, particularly in light of recent studies that have acknowledged an error magnitude of 15%. It is essential to note that this 15% error assessment is derived from real-world testing on stands as opposed to CFD simulations, which inherently possess their margin of error in comparison to actual conditions.

For future work, a coefficient will be added to avoid the actual necessity of modification in the CAD domain. The coefficient will be put under observation for the following turbine projects since it may vary from each turbine's specifications and alter the final results.

ACKNOWLEDGEMENT

This work was supported by the Romanian Research and Development Institute for Gas Turbines COMOTI.

REFERENCES

[1] Genetic algorithm for gas turbine blading design,Cleopatra F. Cuciumita, Valeriu A. Vilag, Valentin Silivestru, Ionut Porumbel, Proceedings of ASME Turbo Expo 2011 GT2011 June 6-10, **2011**, Vancouver, British Columbia, Canada GT2011-46171

[2] Ainley, D. G. and Mathieson, G. C. R., "A Method of Performance Estimation for Axial-Flow Turbines", Aero Res Council Reports and Memoranda no. 2974, **1951**

[3] Smith, S.F., "A Simple Correlation of Turbine Efficiency", J. Royal Aero Soc, vol. 69, no.655, July **1965**, pp. 467-470

[4] Horlock, J. H., "Axial Flow Turbines", Butterworth, **1966**
[5] Latimer, R. J., "Axial Turbine Performance Prediction", Off-Design Performance of Gas Turbines, VKI LS 1978-2, **1978**
[6] Muchatorov, M. Kh. and Krichakin, V. I., "Procedure for Estimating Flow Section Losses in Axial Flow Turbines ehen Calculating their Characteristic", Teploenergetika, vol. 16, no. 7, **1969**, pp. 76-79
[7] Craig, H. R. M. and Cox, H. J. A., "Performance Estimation of Axial Flow Turbines", Proc. Inst. Mech. Engrs, vol. 185, **1970**, pp. 407-424
[8] Liu, Y.; Hendrick, P.; Zou, Z.; Buysschaert, F. A Reliable Update of the Ainley and Mathieson Profile and Secondary Correlations. *Int. J. Turbomach. Propuls. Power* **2022**, *7*, 14.
[9] Liu, Y.M.; Hendrick, P.; Zou, Z.P.; Buysschaert, F. Statistical and Computational Evaluation of Empirical Axial Turbine Correlations in Design of Centrifugal Turbines. *J. Turbomach.* **2021**, *144*, 041002.
[10] Al Jubori, A.M.; Al-Dadah, R.K.; Mahmoud, S.; Daabo, A. Modelling and Parametric Analysis of Small-Scale Axial and Radial-Outflow Turbines for Organic Rankine Cycle Applications. *Appl. Energy* **2017**, *190*, 981–996.
[11] Dunham, J. Loss Mechanisms and Unsteady Flows in Turbomachines. In Proceedings of the Technical Report AGARD-CP-571, Propulsion and Energetics Panel 85th Symposium, Derby, UK, 8–12 May **1995**.
[12] Agromayor, R.; Nord, L.O. Preliminary Design and Optimization of Axial Turbines Accounting for Diffuser Performance. *Int. J. Turbomach. Propuls. Power* **2019**, *4*, 32.
[13] Aungier, R. *Turbine Aerodynamics: Axial-Flow and Radial-Inflow Turbine Design and Analysis*; ASME Press: New York, NY, USA, **2006**.
[14]Dunham, J., & Came, P. M. (1970). Improvements to the Ainley-Mathieson Method of Turbine Performance Prediction. Journal of Engineering for Power, 92(3), 252.
[15] Kacker, S.C.; Okapuu, U. A Mean Line Prediction Method for Axial Flow Turbine Efficiency. *J. Eng. Power* **1982**, *104*, 111–119.
[16] Sieverding, C.; Manna, M. A Review on Turbine Trailing Edge Flow. *Int. J. Turbomach. Propuls. Power* **2020**, *5*, 10.
[17]M.H. Vavra , Aero-thermodynamics and flow in turbomachines. Jhon Wiley & Sons.
[18]Ennio Macchi, Computer program for prediction of axial flow turbine performance. United States Naval Postgraduate School. NPS-57MA70081A. August **1970**.
[19]Stanciu, V., Silivestru, V., Leventiu, C., and Dinu, C., "GazodinamicaTranzitorie a Turbomotoarelor (Gas-turbine engines transient dynamics)", EdituraPrintech, Bucharest, Romania, **2005**, ISBN 973-718-185-9

A DIRECT NUMERICAL SIMULATIONS SOLVER FOR FUNDAMENTAL TURBULENCE AND AEROACOUSTIC RESEARCH

Vlad APARECE-SCUTARIU[1], Valeriu DRAGAN[1]

Received: 18.03.2024
Accepted: 12.05.2024
Published: 18.07.2024
Corresponding author:
vlad.aparece@comoti.ro

ABSTRACT: A Direct Numerical Simulations (DNS) solver is presented, purposely developed for producing high-fidelity simulations in the area of Computational Aeroacoustics for fundamental research. The code has the ability to solve the Navier-Stokes equation in either Cartesian or cylindrical coordinates which are mapped to generalised computational coordinates for ease of derivatives calculation. The solver is 4th-order accurate in space and time. If the cylindrical configuration is considered, a spectral decomposition is used in the azimuthal direction. Spatial and temporal discretisations focus on memory optimisation, reducing the load on current bandwidth-limited High Performance Computing systems. As such, a 7-point compact scheme is used in space with very good performances in terms of resolved wavenumbers and an explicit Runge-Kutta time marching scheme with only two memory registries required per stage, per time-step. An example case of a turbulent round jet is ran with the solver with some key results. These results are very difficult to obtain by experimental means, showing the ability of DNS to accurately capture important flow features. Results show a very good resolution for the jet acoustic field with proper identification of acoustic sources and the propagation of acoustic noise, as well as for the vorticity field with fine vortical structures being captured. Furthermore, the use of DNS allows for easy identification of the turbulent/non-turbulent interface as well as scalar dissipation rate coherent structures in the nozzle vicinity. These quantities are difficult to obtain by experimental means.

KEYWORDS: Direct Numerical Simulations, Computational Aeroacoustics, Turbulence, Turbulent Mixing, High Performance Computing

NOMENCLATURE

CAA	Computational Aeroacoustics
CIC	Characteristic Interface Condition
DNS	Direct Numerical Simulations
ERK	Explicit Runge-Kutta
FD	Finite Difference
HPC	High Performance Computing
HiPSTAR	High Performance Solver for Turbulence and Aeroacoustic Research
ODE	Ordinary Differential Equation
PDE	Partial Differential Equation

[1] Romanian Research and Development Institute for Gas Turbines COMOTI

SDR Scalar Dissipation Rate
TNTI Turbulent/Non-turbulent Interface

1. INTRODUCTION

Widely occurring in nature or man-made environments, turbulence represents the three-dimensional unsteady, apparently random motion of fluid, responsible for a large part of heat transfer and mixing as well as the increase in aerodynamic noise and drag. Despite its wide appearance and importance in many engineering applications, the nature of turbulence is complex and its prediction remains up to date an extremely challenging task. The reason has to do mainly with the presence of a very large range of time and length scales characterising turbulent eddies in the fluid and their interaction across different scales. This range of eddy frequencies and sizes is a function of the Reynolds number, Re. The computational load necessary to resolve all spatial and temporal scales of turbulent flow is approximatively direct proportional to Re^3 [1].

Direct numerical simulations (DNS) represent the process of obtaining the complete solution to the nonlinear, time-dependent Navier-Stokes equations, where all the components (i.e. convective and viscous terms, energy sources or sinks etc.) are being considered. Initial flow solution as well as boundary conditions are specified to carry out precise 'numerical investigations' of physical problems such as turbulence in wall-bounded flows, propagation of acoustic waves, turbulence in wall-bounded flows. These are just a few of the examples where DNS is a useful tool. Although by solving for all time and length scales there is an adverse scaling with the Reynolds number, the reward for doing DNS is the production of reliable flow data, free from any modelling and its uncertainties. In the last decades, DNS have given data which would otherwise require tremendous efforts to obtain via traditional, experimental means. As such, these numerical simulations helped in understanding fundamental phenomena in fluid mechanics [2,3] as well as developing, validating and improving existing turbulence models [4].

As considerable computational resources are necessary for fully resolved turbulent DNS, until recently only idealized flow configurations, with unrealistically small domains and reduced Reynolds numbers have been looked at. Still, the exponential increase in computational capabilities has allowed DNS to work at higher Reynolds numbers, closer to reality, with more practical geometries. The prerequisite for these simulations is, however, the availability of solvers which are able to fully benefit from the latest computational hardware. The aim of this paper is two-fold: (i) to present the capabilities of a DNS solver tailored for modern High Performance Computing (HPC) infrastructure along with key numerical features and parallel performance and to (ii) present results of a DNS investigation carried out on a turbulent steady-state round jet at a Reynolds number of 7290.

2. EXPERIMENTAL SETUP

Originally developed by Prof. Richard Sandberg, the High Performance Solver for Turbulence and Aeroacoustic Research (HiPSTAR) has been continuously developed over the last 17 years, since its birth at the University of Southampton [5], with the latest additions including a chemical-kinetics module [6] as well as the ability to run hydrogen jet flows (development finished). This DNS solver employs a multi-block structured mesh. The Navier-Stokes equations in cylindrical coordinates are solved on a generalised curvilinear grid with a conformal 2D mapping of streamwise and radial components *(x, r) to* general coordinates (η, ξ). As minimisation of computational time has been a key endeavour in the evolution of the solver, the numerical algorithm behind it was developed to meet stringent criteria. These relate to stability of the numerical scheme, efficiency of the scheme (high ratio of numerical accuracy to computational effort), flow features resolution with minimal phase and amplitude errors as well as highly efficient parallelisation on modern HPC systems.

An effective method to increase performance of a numerical solver on modern, limited bandwidth HPC architectures is to cut on memory requirements as much as possible, for a given simulation. The present DNS solver achieves this by using a 7-point stencil parallel 4^{th}-order accurate compact finite difference numerical scheme in the spatial domain with wavenumber optimisation [7] (Figure 1) which obtains the same level of accuracy as a traditional explicit scheme with a lower number of mesh points. This is desirable, especially for Computational Aeroacoustics (CAA) studies, where there is a need to capture a wide spectrum of aerodynamic noise. Such noise has a large broadband characterised by amplitudes of flow variables significantly smaller than mean quantities. Although FD schemes do not reach the high resolution of spectral methods, nowadays, increasingly high-order FD prove to be suitable for areas like CAA. Yet, the main

difficulty of implementing these high-order schemes is the boundary treatment. Since there are stringent requirements on the accuracy of calculation for flux quantities, this desired accuracy has to be maintained at the boundaries. It has been determined [8] that n-order schemes for hyperbolic partial differential equations must be closed with at least (n-1)-order accurate schemes in order to maintain accuracy in space. The compact scheme used in the present DNS solver has very low dispersion and dissipation as it is required for the numerical solution to remain accurate over a long propagation distance from the noise source. The 7-point stencil compact scheme has a pentadiagonal matrix system of the form:

$$f_i^{'} + \alpha(f_{i-1}^{'} + f_{i+1}^{'}) + \beta(f_{i-2}^{'} + f_{i+2}^{'}) = \frac{1}{h}\sum_{m=1}^{3} a_m(f_{i+m} - f_{i-m}) \quad (1)$$

where $1 < i < N-1$ with the coefficients α, β and $a_{m=1...3}$ given in Table 1.

Table 1: Coefficients for the interior points of the compact scheme

α	0.5862704032801503
β	0.09549533555017055
a_1	0.6431406736919156
a_2	0.2586011023495066
a_3	0.007140953479797375

Assessment of the compact scheme at high wavenumbers is performed in the spectral-domain [7]. The discrepancy between analytical and numerical results is analysed for a sinusoidal function with changing size of the mesh (Δx). Fourier transformation of Eq. 1 leads to:

$$i\kappa_n\hat{f}(k)[1 + 2\alpha\cos(\kappa_t) + 2\beta(2\kappa_t)] = 2i\hat{f}(k)\int_{m=1}^{3} a_m\sin(m\kappa_t) \quad (2)$$

where κ_t is the analytical or true wavenumber, scaled by the mesh size (i.e. $\kappa_t=k_t\Delta x$) and κ_n is the numerical approximation (i.e. $\kappa_n=k_n\Delta x$). A compact scheme with high resolution would require κ_n to match κ_t up to very large values. Resolution capabilities for the compact scheme used in the present DNS solver is shown in Figure 1. The value of κ_n will ultimately go to 0 for $k=\pi$, highlighting the final limit of finite differentiation.

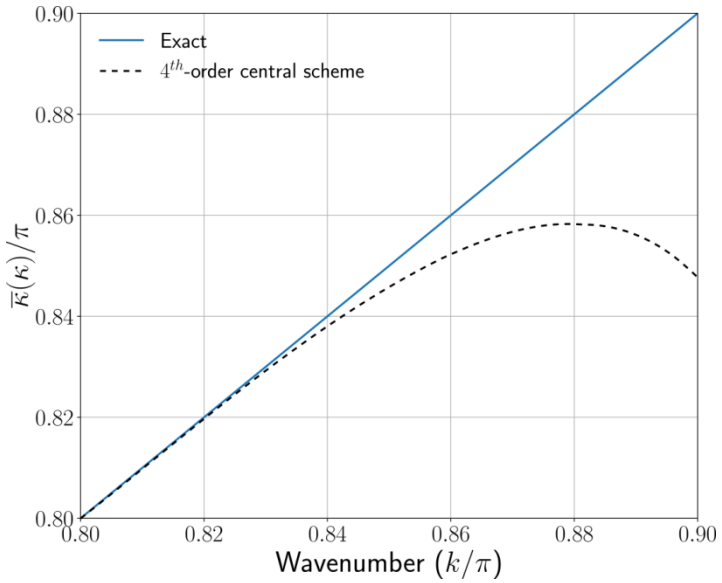

Figure 1. Resolution of the modified wavenumber for the 4th-order central differencing, pentadiagonal, compact scheme

In terms of boundary treatment, for the present DNS solver, the approach of Carpenter *et al.*, [9] is used for constructing accurate compact one-sided boundary closures. These meet the stability criteria of Gustafsson *et al.*, [10] for numerical boundary conditions while maintaining asymptotic stability.

For time-marching, the present DNS solver makes use of a low memory storage explicit Runge-Kutta (ERK) scheme. As DNS aims to solve for all relevant time and length scales, it might be that billions of points are needed for obtaining a high-fidelity flow field [11]. This implies a significant memory load, putting a constraint on time integration to be accurate enough for the spatial discretisation used. Yet, the integration should require minimum fast-access memory. Even though current HPC-machines are built with considerable memory capabilities, the use of low-storage ERK schemes is still necessary for compressible DNS solvers. Given the compressible Navier-Stokes equations, as a set of coupled partial differential equations, these can be discretised using the method-of-lines, becoming coupled ordinary differential equations (ODEs), giving an initial-value boundary problem of the kind:

$$\frac{\boldsymbol{dU}}{\boldsymbol{dt}} = \boldsymbol{R}(\boldsymbol{t}, \boldsymbol{U}(\boldsymbol{t})) \qquad \boldsymbol{t} \in [\boldsymbol{a}, \boldsymbol{b}] \qquad \boldsymbol{U}(\boldsymbol{t_0}) = \boldsymbol{U_0} \tag{3}$$

where **U** represents the vector of conservative variables (ρ, $\rho\mathbf{u}$, ρE …) and **R** contains the right-hand-side terms of the Navier-Stokes equations (i.e. advection, diffusion, viscous stresses etc.). A general s-stage RK scheme has the form:

$$\begin{gathered} \boldsymbol{t^{(i)}} = \boldsymbol{t^{(n)}} + \boldsymbol{c_i \Delta t} \qquad \boldsymbol{R^{(i)}} = \boldsymbol{R^{(i)}}(\boldsymbol{t^{(i)}}, \boldsymbol{U^{(i)}}), \\ \boldsymbol{k^{(i)}} = \boldsymbol{R}(\boldsymbol{t^{(n)}} + \boldsymbol{c_i \Delta t}, \boldsymbol{U^{(n)}} + \boldsymbol{\Delta t} \sum_{\boldsymbol{j=1}}^{\boldsymbol{i-1}} \boldsymbol{a_{ij} R^{(j)}}), \\ \boldsymbol{U^{(n+1)}} = \boldsymbol{U^{(n)}} + \boldsymbol{\Delta} \sum_{\boldsymbol{i=1}}^{\boldsymbol{s}} \boldsymbol{b_i k_i}, \end{gathered} \tag{4}$$

where $R^{(i)}$ is the RHS of the Navier-Stokes equations at $t^{(i)}$, $k^{(i)}$ is an increment defined as the function of slope at point $t^{(i)}$, based on $U^{(n)}$ and R at $t^{(i-1)}$. The Butcher coefficients a_{ij}, b_j and c_i can be given in the form:

$$\begin{array}{c|c} \mathbf{M} & \boldsymbol{\Lambda} \\ \hline & \boldsymbol{\Theta} \end{array}, \tag{5}$$

where **M** is the column vector $(c_0, c_1, c_2, \ldots, c_{s-1})$ with $\sum_{j=1}^{i-1} a_{ij} = c_i$, $\boldsymbol{\Lambda}$ is the lower triangular square matrix containing a_{ij} terms, $\boldsymbol{\Theta}$ is a row vector $(b_0, b_1, b_2, \ldots, b_{s-1})$. Coefficients a_{ij}, b_j and c_i are constrained by equations of condition [12]. Straightforward application of Eq. 4 would require s+1 memory registers with length N, where N is the ODE number. The main objective of low-storage ERK time-marching schemes is to reduce the number of memory registers required, through algebraic relations between the Butcher coefficients. This is carried out in order to store only certain intermediate ERK stages, rather than the entire s+1 set. Williamson [13] demonstrated that 2-register implementation can be produced for all ERK schemes of 2nd order, a considerable amount of 3rd order ones and a few 4th order schemes. For the latter, these implementations restrict the cases where R(t,U) stays bounded, as $U \rightarrow \infty$. The 2-registers approach can be detailed as:

$$\begin{gathered} \textbf{Register 1: } \boldsymbol{Q^{(i)}} = \boldsymbol{A_i Q^{(i-1)}} + (\boldsymbol{\Delta t}) \boldsymbol{R^{(i)}}, \\ \textbf{Register 2: } \boldsymbol{U^{(i)}} = \boldsymbol{U^{(i-1)}} + \boldsymbol{B_i Q^{(i)}}, \end{gathered} \tag{6}$$

where A_i and B_i are functions dependent on the Butcher coefficients with $A_1=0$; $Q^{(i-1)}$ and $U^{(i-1)}$ are overwritten successively in memory with $Q^{(i)}$ and $U^{(i)}$. Alternatively, Wray [14] created a 2-register scheme, using the stability analysis for ERK schemes of van der Houwen [15]:

$$\begin{gathered} \textbf{Register 1: } \boldsymbol{U^{(i+1)}} = \boldsymbol{Q^{(i)}} + (\boldsymbol{a_{i+1,i}}) \boldsymbol{\Delta t R^{(i)}}, \\ \textbf{Register 2: } \boldsymbol{Q^{(i+1)}} = \boldsymbol{U^{(i+1)}} + (\boldsymbol{b_i} - \boldsymbol{a_{i+1,i}}) \boldsymbol{\Delta t R^{(i)}}, \\ \textbf{Register 2: } \boldsymbol{U^{(i+2)}} = \boldsymbol{Q^{(i+1)}} + (\boldsymbol{a_{i+2,i+1}}) \boldsymbol{\Delta t R^{(i+1)}}, \\ \textbf{Register 1: } \boldsymbol{Q^{(i+2)}} = \boldsymbol{U^{(i+2)}} + (\boldsymbol{b_{i+1}} - \boldsymbol{a_{i+2,i+1}}) \Delta \boldsymbol{t R^{(i+1)}} \end{gathered} \tag{7}$$

where Q is "an information carrier" from the previous stage to the present one and a_{ij}, b_i are the Butcher coefficients. The important difference between Williamson's [14] and Wray's [13] implementations is that during evaluations of terms at a given time-step in Eq. 7, the vector with the previous solution is overwritten.

Where this is not acceptable, the method proposed by Williamson is the only choice. Still, for compressible DNS, the Wray implementation is appropriate as **U** is decomposed into primitive variables which are needed to calculate flux terms (i.e. in **R**), such that **U** becomes redundant. Reduction in memory for the Wray scheme has the cost of losing U at the previous time-step. This reduced the possibility of error control, if time integration is not within the error bounds. To correct for this, an extra memory registry is needed for U. The present DNS solver has a 2-registry, 5-stage, 4th-order accurate ERK with the Butcher coefficients as [16]:

Table 2: Butcher coefficients for the ERK implemented in the present DNS solver [16]

$c_2 = \frac{9702866171893}{4311952581923}$	$a_{21} = \frac{9702866171893}{4311952581923}$
$c_3 = \frac{6584761158862}{12103376702013}$	$\cancel{a_{31}},\ a_{32} = \frac{6584761158862}{12103376702013}$
$c_4 = \frac{2251764453980}{15575788980749}$	$\cancel{a_{41}},\ \cancel{a_{42}},\ a_{43} = \frac{2251764453980}{15575788980749}$
$c_5 = \frac{26877169314380}{34165994151039}$	$\cancel{a_{51}},\ \cancel{a_{52}},\ \cancel{a_{53}},a_{54} = \frac{26877169314380}{34165994151039}$
	$b_1 = \frac{1153189308089}{22510343858157},\ b_2 = \frac{1772645290293}{4653164025191},\ b_3 = -\frac{1672844663538}{4480602732383}$
	$b_4 = \frac{2114624349019}{3568978502595},\ b_5 = \frac{5198255086312}{14908931495163}$

Appropriate spatial and temporal discretisation is necessary for capturing the entire broadband of aeroacoustic noise. Yet, in the context of a multi-block approach, used in the present DNS solver, it is necessary to also have an accurate communication between neighbouring mesh blocks such that the flow solution is propagated correctly, without artificial dissipation or dispersion. Characteristic interface conditions [17] are able to handle such computational domain discontinuities. Given the use of high-order finite difference (FD) discretisations of the governing equations, such discontinuities are a source of suprious oscillations. In the CIC method, two neighbouring blocks are isolated along their singularity line (i.e. interface) and a set of high-order one sided FD at points in the interface vicinity. At the interface, characteristic boundary conditions are imposed (Figure 2), based on the Navier-Stokes Characteristic Boundary Conditions [18].

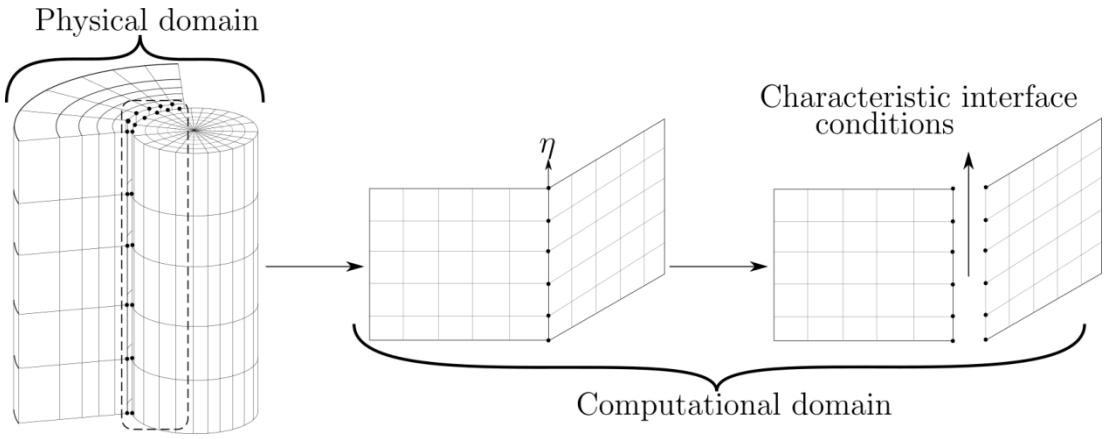

Figure 2. Block interfaces treatment using boundary conditions, based on characteristic relations of the Navier-Stokes equations at a constant η coordinate line

A singularity line in 2D generalised coordinates (η, ξ) are defined by the relation:

$$\lim_{\eta \to c^+} \nabla \boldsymbol{\eta} \neq \lim_{\eta \to c^-} \nabla \boldsymbol{\eta}, \tag{8}$$

where c is a constant coordinate line, η=c, while c^+ and c^- represent the limits approaching from the left hand side (LHS) and right hand side (RHS). Despite that the singularity is defined by different LHS and RHS limits, normalised vector magnitudes are equal:

$$\lim_{\eta \to c^+} \frac{\nabla \eta}{|\nabla \eta|} = \lim_{\eta \to c^-} \frac{\nabla \eta}{|\nabla \eta|}, \tag{9}$$

The characteristic wave equation at the interface, assuming Local-One-Dimensional-Decomposition [18] can be written as:

$$\frac{\partial \boldsymbol{R}}{\partial t} + \bar{\boldsymbol{\lambda}} \frac{\partial \boldsymbol{R}}{\partial \eta} = \boldsymbol{S}_c, \tag{10}$$

with modified wave velocities λ_i, due to the transformation in generalised coordinates:

$$\bar{\boldsymbol{\lambda}} = (\boldsymbol{U}, \boldsymbol{U}, \boldsymbol{U}, \boldsymbol{U} + \boldsymbol{c}\sqrt{\boldsymbol{\eta}_z^2 + \boldsymbol{\eta}_r^2}, \boldsymbol{U} - \boldsymbol{c}\sqrt{\boldsymbol{\eta}_z^2 + \boldsymbol{\eta}_r^2})^T \tag{11}$$

where $\eta_z = \partial\eta/\partial\eta$ and $\eta_r = \partial\eta/\partial r$.

At the boundaries of the computational domain, incoming waves are undesirable [18]. At the interface between two neighbouring blocks, any incoming wave for an isolated block should be compensated by an outgoing wave from an adjacent block. This implies the primitive variables at the interface on the LHS and RHS should be equal:

$$(\boldsymbol{\rho}^{\mathbf{L}}, \mathbf{u}^{\mathbf{L}}, \mathbf{p}^{\mathbf{L}}) = (\boldsymbol{\rho}^{\mathbf{R}}, \mathbf{u}^{\mathbf{R}}, \mathbf{p}^{\mathbf{R}}), \tag{12}$$

and if Eq. 9 and Eq. 11 are taken into account, variation in time of the characteristic wave amplitude should be the same:

$$\frac{\partial \boldsymbol{R}^{\boldsymbol{L}}}{\partial t} = \frac{\partial \boldsymbol{R}^{\boldsymbol{R}}}{\partial t}, \tag{13}$$

or if the spatial wave variation is considered in Eq. 10:

$$\bar{\boldsymbol{\lambda}} \frac{\partial \boldsymbol{R}^{\boldsymbol{L}}}{\partial \eta} - \boldsymbol{S}_c^{\boldsymbol{L}} = \bar{\boldsymbol{\lambda}} \frac{\partial \boldsymbol{R}^{\boldsymbol{R}}}{\partial \eta} - \boldsymbol{S}_c^{\boldsymbol{R}}, \tag{14}$$

Condition in Eq. 13 is achieved by passing spatial information through the interface using Eq. 14. The convention when establishing incoming and outgoing waves is to follow the direction of the characteristic velocity λ_i. As a result, a negative velocity highlights a wave traveling from right to left and vice-versa for a positive velocity. It follows that an outgoing wave remains unchanged, while an incoming wave needs to be corrected:

$$\begin{aligned} \bar{\boldsymbol{\lambda}} \frac{\partial \boldsymbol{R}^{\boldsymbol{L}}}{\partial \eta} &= \bar{\boldsymbol{\lambda}} \frac{\partial \boldsymbol{R}^{\boldsymbol{R}}}{\partial \eta} - \boldsymbol{S}_c^{\boldsymbol{R}} + \boldsymbol{S}_c^{\boldsymbol{L}}, \quad && \textbf{for} \quad \boldsymbol{\lambda_i \leq 0} \\ \bar{\boldsymbol{\lambda}} \frac{\partial \boldsymbol{R}^{\boldsymbol{R}}}{\partial \eta} &= \bar{\boldsymbol{\lambda}} \frac{\partial \boldsymbol{R}^{\boldsymbol{L}}}{\partial \eta} - \boldsymbol{S}_c^{\boldsymbol{L}} + \boldsymbol{S}_c^{\boldsymbol{R}}, \quad && \textbf{for} \quad \boldsymbol{\lambda_i \geq 0} \end{aligned} \tag{15}$$

3. DNS OF A TURBULENT STEADY-STATE ROUND JET AND IDENTIFICATION OF ACOUSTIC SOURCES

In this section, turbulent mixing of a passive species is investigated in a steady-state jet using the presented DNS solver, HiPSTAR. Statistical convergence of the simulation is evaluated, higher-order Reynolds stresses are validated with experimental measurements and the turbulent/non-turbulent jet interface is quantified. Alongside this, the versatility of spatial and temporal discretisation is assessed to capture the wide broadband spectrum of aeroacoustic noise as well as the fine vortical structures present in the flow. Production of DNS data using the solver was carried out on the ARCHER supercomputer in the United Kingdom, using between 512 and 1024 cores and an approximatively total computational time of 168 hours.

3.1 Flow configuration and grid convergence

Domain configuration for the steady-state jet simulation is described in Figure 3. The domain is stretched in the axial direction, spanning 60D, while in the radial direction it is 30D wide, where D is the jet inlet diameter. Reynolds number at the inlet is 7300, while the flow remains subsonic (Mach number 0.35). Temperature is kept constant at 300K. A top-hat velocity profile is imposed at the inlet with weak turbulent fluctuations (5% turbulence intensity). Turbulence is created using an artificial turbulence generator, based on the work of Kempf *et al.*, [19]. This eliminates the need of additional mesh before the inlet, that would be required for turbulence to develop and instead, recreates fluctuations based on prescribed Reynolds stresses from experimental measurements. At the outlet, a Navier-Stokes non-reflecting boundary condition (NSCBC) is imposed [18] with a 15 points zonal boundary [20] at the outlet vicinity, to dampen nonphysical reflections that come back into the flow domain. To fully resolve all turbulent and mixing scales, the grid size needs to be close to the Kolmogorov and Obukhov-Corrsin scales:

$$l_k = \left(\frac{\nu^3}{\epsilon}\right)^{1/4}, \qquad \lambda_{O-C} = l_k Sc^{-3/4}, \tag{16}$$

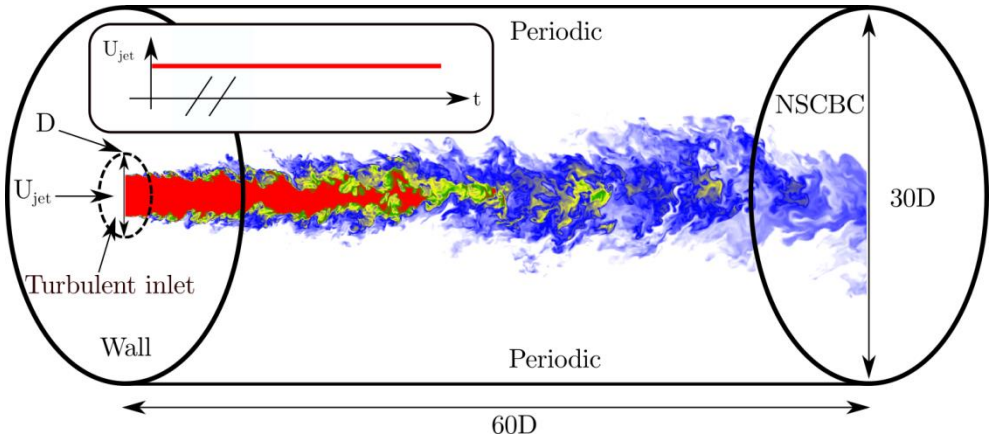

Figure 3. The flow configuration for the steady-state jet

These are similar for flow Schmidt numbers lower than 1. Moin and Maesh [21] argued that for DNS simulations focusing on turbulence, grid resolution requirements can be relaxed as long as $\Delta \approx O(\eta)$. Good agreement between experimental and numerical results was obtained for $\Delta/l_k \approx 2.1$ [22] and $\Delta/l_k \approx 4.5$ [21] considering isotropic turbulence. Figure 4 shows the ratio of grid spacing to Kolmogorov/Obukhov-Corrsin. As turbulent scales change in the axial direction (Figure 4a), grid spacing increases from $\approx 0.3l_k$ in the inlet vicinity, to $\approx 0.8l_k$ around x/D=10. The resolution remains below the $2.1l_k$ value used by Yeung and Pope [22]. Mixing scales (Figure 4c) follow the same trendline, with grid resolution closer to the theoretical mixing scale. If the radial direction is considered, turbulent scales have a better resolution (Figure 4b), while length scales associate with mixing length remain under the Obukhov-Corrsin limit (Figure 4d).

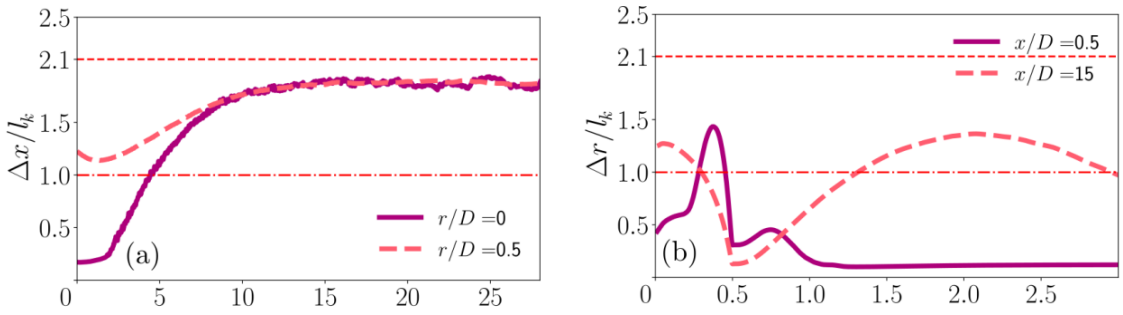

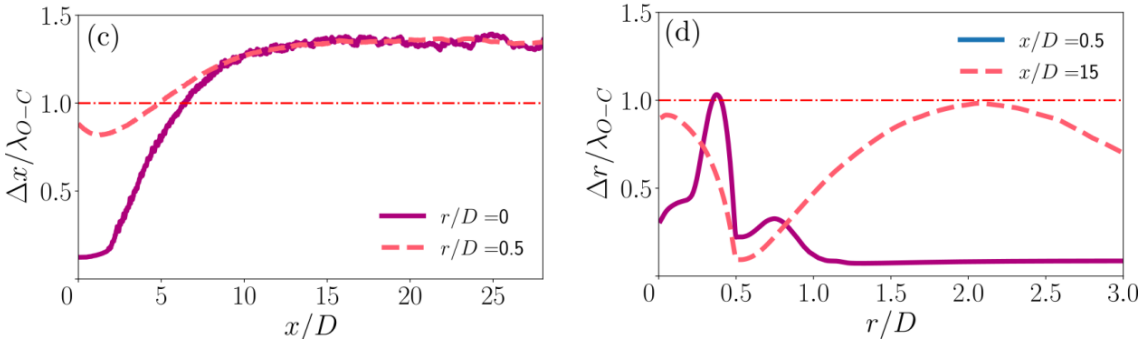

Figure 4. Grid resolution of DNS in (a) axial and (b) radial directions, as compared to Kolmogorov scale and (c), (d) compared to the Obukhov-Corrsin mixing scale.

Besides the grid resolution investigation, another important flow validation relates to the extent to which the Kolmogorov spectra is captured, from integral scales to the smallest turbulent eddies. Spatial information on turbulence can be inferred from data time-series, by using Taylor's hypothesis [23]. In this case axial velocity is selected since it has the highest mean magnitude. To obtain the spectra for turbulent energy and mixing energy, the time-series domain is split into three windows of equal size. Frequencies (f) are transformed into the wavenumber domain with $\kappa = 2\pi f/\overline{u}$ and $\kappa = 2\pi f/\overline{\xi}$, where $\overline{u}$ is the mean axial velocity and $\overline{\xi}$ is the mixture fraction of the passive species released in the flow. Turbulent energy and passive scalar spectra are illustrated in Figure 5a with their corresponding dissipation spectra shown in Figure 5b. The estimated dissipation rate is calculated by assuming isotropy of turbulence as $\epsilon \approx 15\nu\overline{(\partial_t u')^2}/\overline{u^2}$. The highest magnitude of turbulent energy spectrum is at κl_k=0.01. In the wavenumber range κl_k=0.07 – 2, the "-5/3" scaling law is visible, a proof of locally isotropic flow. The same "-5/3" law is observable in the case of the scalar spectrum, confirming the similarity between the two spectra for sub-unity Schmidt numbers (gaseous flows). The wavenumber range demonstrates that the smallest turbulent and turbulent mixing scales are resolved. Moreover, it shows that while there is a correlation between large eddies and high turbulent energy, dissipation occurs at the smaller eddies, close to the diffusion limit.

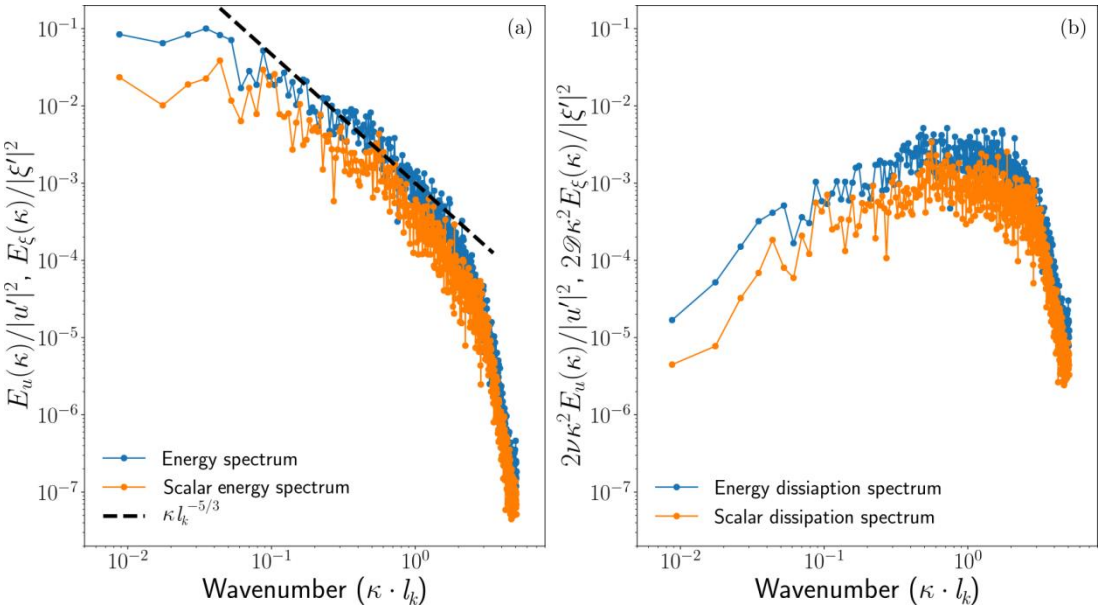

Figure 5. Spectra of (a) energy and (b) dissipation in the steady-state turbulent jet

3.2. DNS results

Assessing the ability of the DNS solver to capture the acoustic jet field as well as the fine vortical structures of turbulence is one of the key objectives of this analysis. Figure 6 shows the mid-plane slice containing the small pressure fluctuations of the steady-state jet which are smoothly captured by the high-order discretisation schemes. The visible spherical waves propagating from jet nozzle shows that acoustic sources

are gathered around the shear layer in the inlet vicinity. The peak amplitude occurs at 45° angles with respect to the jet centreline axis, agreeing with existing literature [24].

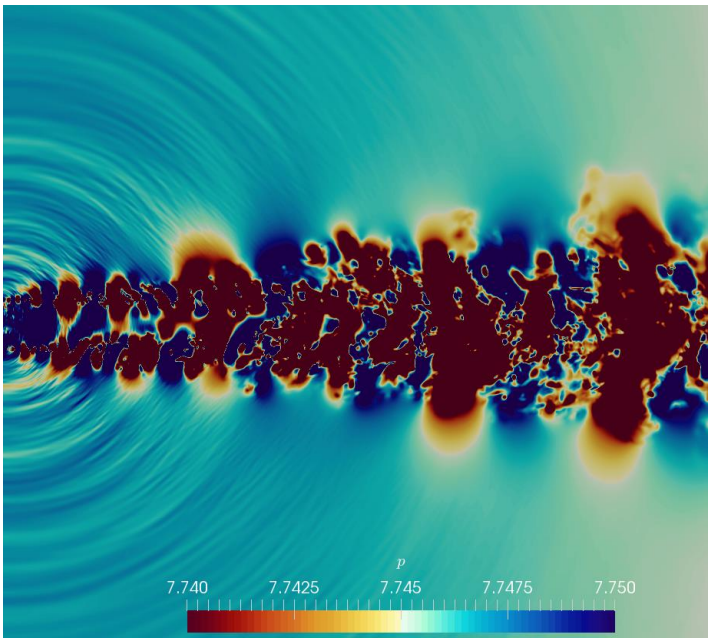

Figure 6. Acoustic sources and their propagation in the turbulent jet, represented using non-dimensionalised pressure variations

Another important flow feature that can be easily analysed with DNS is the turbulent/non-turbulent jet interface (TNTI). Mechanics of the TNTI which separates the continuous jet area from the ambient fluid received considerable attention in the past with notable investigations such as those of Corrsin and Kestler [25] and Wygnanski and Fiedler [26]. Large-eddies motion generates large-scale bulges which are increasing in size with downstream distance and so does the amplitude of wave-like structures which represent the interface. As the turbulent area, characterised by rotational fluid expands, it engulfs ambient irrotational air. This phenomenon occurs through the action of viscous shear forces, caused by the smallest eddies. Figure 7 shows the instantaneous vorticity field on which an intermittency factor for the jet boundary is condition. The figure illustrates jet evolution from the area of the potential core (x/D<5) to a fully developed turbulent flow downstream. Vortical structures are initially formed in the shear layers near the inlet, merging eventually at the end of the potential core area. An increase in length scales characteristic for turbulence can be noticed.

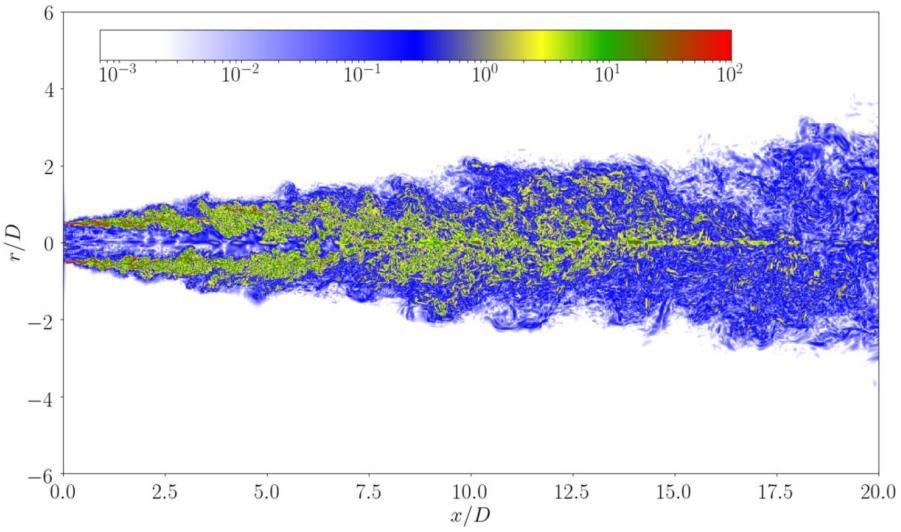

Figure 7. Middle-plane slice of the instantaneous vorticity field.

Figure 8 shows the intermittency factor (γ) for the present jet. This is given as the probability of vorticity to be higher than a specific threshold. Despite the fact there is no consensus in defining the threshold, the present DNS simulation considers the recommendation of Phillips [27]. This relates second-order velocity correlations in the proximity of the TNTI and is experimentally validates [28,29]:

$$\overline{v'^2} = \overline{u'^2} + \overline{w'^2}, \tag{17}$$

Self-similarity for the intermittency factor is observed after x/D=20. The value signifying the beginning of the TNTI is determined as 0.96 γ [30]. DNS results are compared with experimental data of Wygnanski and Fiedler [26] (hereafter referred to as WF69). They have used a direct counting method, relying on first and second time derivatives of axial velocity. This method measured the time fraction when the flow is turbulent, in the area where the TNTI was observed visually. Intermittency factor decay starts at a location that is further away from the jet centreline as compared to WF69. This suggests the TNTI is less developed in the present DNS jet. Moreover, present data reveals a steeper decay for γ. This is explained by the differences in length of the potential core. For present DNS, intermittency achieves a self-similar state after x/D=20, while WF69 investigates the intermittency after x/D=90. WF69 benefits from a longer flow "domain", as its Reynolds number is of the order of 10^5, compared to 7290 for the present case. It is worth remembering the computational effort for DNS increases approximatively with Re^3. Still the TNTI profiles are reasonably close. The TNTI thickness is given as the radial distance over which γ decays from 0.96 to 0. Differences in this thickness between present DNS and WF69 are mostly a consequence of the difference in the characteristic length scale of vorticity fluctuations with which TNTI thickness scales in the jet [31].

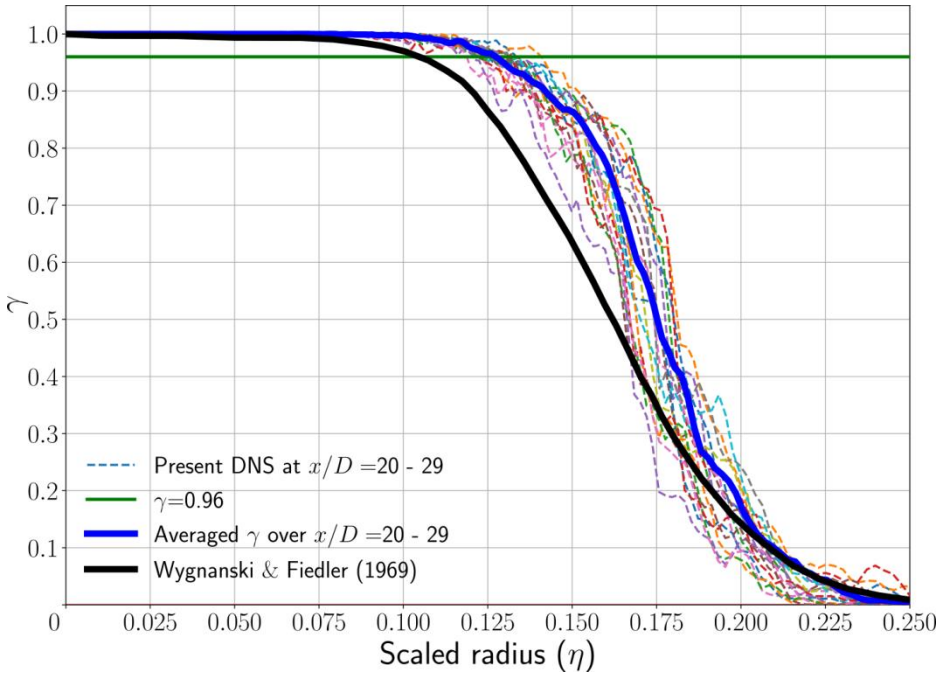

Figure 8. Intermittency factor (γ) radial profiles for the turbulent jet, a comparison between DNS and direct measurements of Wygnanski and Fiedler [26].

DNS facilitates a direct evaluation of the scalar dissipation rate (SDR) and its axial, radial and azimuthal components. The SDR is an important quantity, alongside the mixture fraction, used in describing any mixing process from turbulent mixing to non-premixed combustion [32]. The SDR quantifies the rate of scalar mixing at molecular scales. Usually denoted as χ, the SDR is a completely defined physical quantity, meaning that it exists at a given point in space and time in a scalar mixing field. This means that its statistics are given in the same way as for other important turbulent flow-related quantities such as turbulent kinetic energy, turbulent energy dissipation etc. The SDR is defined as:

$$\chi = 2\alpha(\nabla\xi \cdot \nabla\xi), \tag{18}$$

where α is the mass diffusivity. Using DNS data, coherent structures of SDR in the jet nozzle vicinity are analysed. It is very difficult to obtain 3D data of SDR in the nozzle vicinity by experimental means. Figure 9a-c shows the near-nozzle structure of SDR components. The radial component of SDR seems to follow a sheet-like arrangement, similar as that for the total SDR. The axial and azimuthal components show three-dimensional irregular structures of high dissipation. The azimuthal component combines axially and azimuthally oriented thin structures of intense dissipation, which can be assumed to be one-dimensional.

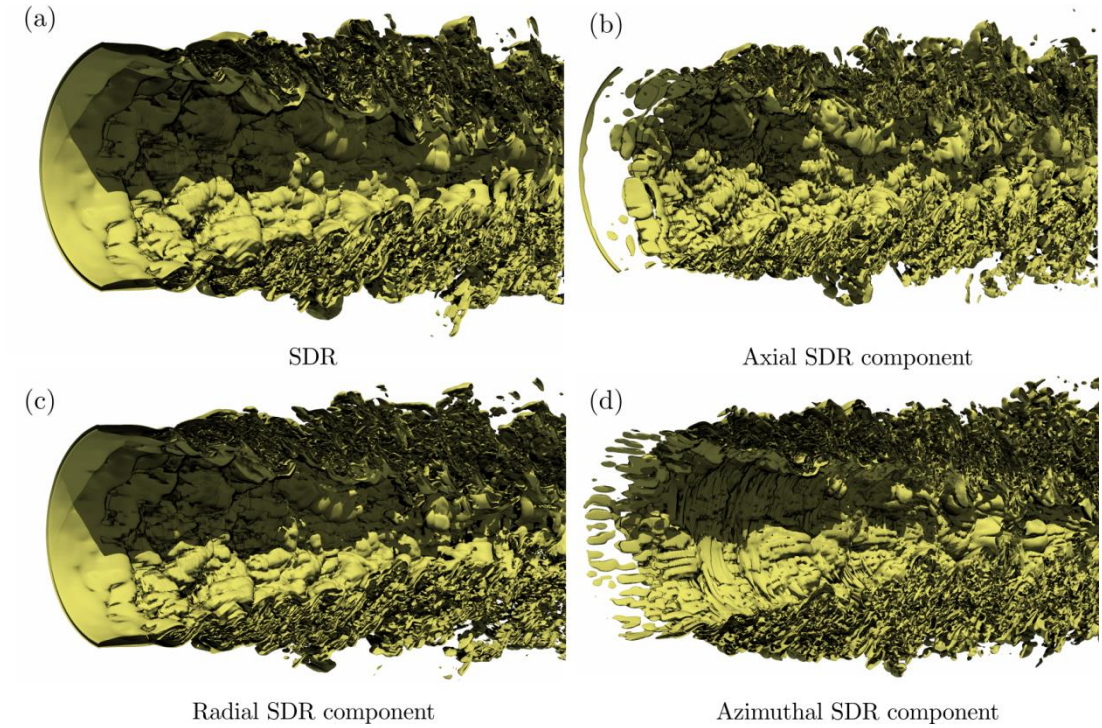

Figure 9. Bird's eye view of high dissipation coherent structures in the near-field of instantaneous (a) SDR, and its (b) axial component, $2\alpha\left(\frac{\partial\xi}{\partial x}\right)^2$, (c) radial component, $2\alpha\left(\frac{\partial\xi}{\partial r}\right)^2$, and (d) azimuthal component, $2\alpha\left(\frac{1}{r}\frac{\partial\xi}{\partial\theta}\right)^2$

4. CONCLUSIONS

A Direct Numerical Simulations (DNS) solver is presented, purposely developed for producing high-fidelity simulations in the area of Computational Aeroacoustics. The code has the ability to solve the Navier-Stokes equation in either Cartesian or cylindrical coordinates which are mapped to generalised computational coordinates for ease of derivatives calculation. The solver is 4th-order accurate in space and time. If the cylindrical configuration is considered a spectral decomposition is used in the azimuthal direction. Spatial and temporal discretisations focus on memory optimisation, reducing the load on current bandwidth-limited High Performance Computing systems. As such, a 7-point compact scheme is used in space with very good performances in terms of resolved wavenumbers, an explicit Runge-Kutta time marching scheme with only two memory registries required per stage, per time-step. An example case of a turbulent round jet is ran with the solver with some key results. These results are very difficult to obtain by experimental means, showing the ability of DNS to accurately capture important flow features. Results show a very good resolution for the jet acoustic field with proper identification of acoustic sources and the propagation of acoustic noise, as well as for the vorticity field with fine vortical structures being captured. Furthermore, the use of DNS allows for easy identification of the turbulent/non-turbulent interface as well as scalar dissipation rate coherent structures in the nozzle vicinity. These quantities are difficult to obtain by experimental means.

The characteristics of a Direct Numerical Simulations solver for computational aeroacoustic research was presented. The solver is highly parallel and employs versatile numerical recipes for increasing its efficiency, while maintaining high-order accuracy. In the context of current bandwidth-limited High Performance Computing systems, the development of the solver focused on memory reduction techniques.

These allow for running turbulent flow simulations at Reynolds numbers closer to those found in real configurations. The solver is 4th-order accurate in space and time with a 7-point compact scheme with very good performance for high wavenumbers and an explicit Runge-Kutta time marching scheme with only two memory registries needed per stage, per time-step. A relevant case study of a turbulent round jet is ran using the DNS solver. Key flow features are described such as evolution of acoustic noise, development of the vorticity field with the fine vortical structures, identification of the turbulent/non-turbulent interface as well as coherent structures of the scalar dissipation rate in the jet nozzle vicinity.

ACKNOWLEDGEMENT

This research was performed within the ”Nucleu” Programme, part of the National Plan for Research, Development and Innovation 2022-2027, carried out with the support of the Romanian Ministry of Research, Innovation and Digitalisation, project no. PN23.12.02.01. Financial support from the Engineering and Physical Sciences Research Council, UK, grants EP/N509644/1, EP/R029369/1 and UKCTRF grant EP/L002698/1 is also gratefully acknowledged.

REFERENCES

[1] Davidson, P. A. 2015. Turbulence: an introduction for scientists and engineers. Oxford University Press.
[2] Kim, J., Moin, P., & Moser, R. Turbulence statistics in fully developed channel flow at low Reynolds number. *Journal of Fluid Mechanics*, 1987, *177*, pp. 133-166.
[3] Freund, J. B. Noise sources in a low-Reynolds-number turbulent jet at Mach 0.9. *Journal of Fluid Mechanics*, 2001, 438, pp. 277-305.
[4] Spalart, P. R. Direct simulation of a turbulent boundary layer up to R_θ=1410. *Journal of Fluid Mechanics*, 1988, 187, pp. 61-98.
[5] Edwards, T., & Sandberg, R. D. Parallelising HiPSTAR using OpenMP. Cray Centre of Excellence for HECToR, Edinburgh, UK, 2011, www. hector. ac. uk/coe/pdf/HiPSTAR_OMP_Report. Pdf.
[6] Aparece-Scutariu, V. Investigation on spatial and temporal characteristics of scalar dissipation rate in non-reacting and reacting turbulent jets. 2021, PhD Thesis.
[7] Kim, J. W. (2007). Optimised boundary compact finite difference schemes for computational aeroacoustics. *Journal of Computational Physics*, 225(1), 995-1019.
[8] Gustafsson, B. (1975). The convergence rate for difference approximations to mixed initial boundary value problems. *Mathematics of Computation*, 29(130), 396-406.
[9] Carpenter, M. H., Gottlieb, D., & Abarbanel, S. (1993). Stable and accurate boundary treatments for compact, high-order finite-difference schemes. *Applied Numerical Mathematics*, 12(1-3), 55-87.
[10] Gustafsson, B., Kreiss, H. O., & Sundström, A. (1972). Stability theory of difference approximations for mixed initial boundary value problems. II. *Mathematics of Computation*, 26(119), 649-686.
[11] de Frahan, M. T. H., Esclapez, L., Rood, J., Wimer, N., Mullowney, P., Perry, B. A., ... & Chen, J. H. (2024). The Pele Simulation Suite for Reacting Flows at Exascale. Oak Ridge National Laboratory (ORNL), Oak Ridge, TN (United States).
[12] Butcher, J. C. (1987). The numerical analysis of ordinary differential equations: Runge-Kutta and general linear methods. Wiley-Interscience.
[13] Williamson, J. H. (1980). Low-storage runge-kutta schemes. *Journal of Computational Physics*, 35(1), 48-56.
[14] Wray, A. A. Minimal Storage Time Advancement Schemes for Spectral Methods. NASA Ames Research Centre, California, Report No. M, 202, 1990.
[15] Van der Houwen, P. J. (1972). Explicit Runge-Kutta formulas with increased stability boundaries. *Numerische Mathematik*, 20(2), 149-164.
[16] Kennedy, C. A., Carpenter, M. H., & Lewis, R. M. (2000). Low-storage, explicit Runge–Kutta schemes for the compressible Navier–Stokes equations. *Applied Numerical Mathematics*, 35(3), 177-219.
[17] Kim, J. W., & Lee, D. J. (2003). Characteristic interface conditions for multiblock high-order computation on singular structured grid. *AIAA Journal*, 41(12), 2341-2348.
[18] Poinsot, T. J. A., & Lelef, S. K. (1992). Boundary conditions for direct simulations of compressible viscous flows. *Journal of Computational Physics*, 101(1), 104-129.
[19] Kempf, A. M., Wysocki, S., & Pettit, M. (2012). An efficient, parallel low-storage implementation of Klein’s turbulence generator for LES and DNS. *Computers & Fluids*, 60, 58-60.

[20] Sandberg, R. D., & Sandham, N. D. (2006). Nonreflecting zonal characteristic boundary condition for direct numerical simulation of aerodynamic sound. *AIAA Journal*, 44(2), 402-405.
[21] Moin, P., & Mahesh, K. (1998). Direct numerical simulation: a tool in turbulence research. *Annual Review of Fluid Mechanics*, 30(1), 539-578.
[22] Yeung, P. K., & Pope, S. B. (1989). Lagrangian statistics from direct numerical simulations of isotropic turbulence. *Journal of Fluid Mechanics*, 207, 531-586.
[23] Taylor, G. I. (1938). The spectrum of turbulence. Proceedings of the Royal Society of London. Series A-Mathematical and Physical Sciences, 164(919), 476-490.
[24] Bodony, D. J., & Lele, S. K. (2008). Current status of jet noise predictions using large-eddy simulation. *AIAA Journal*, 46(2), 364-380.
[25] Corrsin, S., & Kistler, A. L. (1955). Free-stream boundaries of turbulent flows (No. NACA-TR-1244).
[26] Wygnanski, I., & Fiedler, H. (1969). Some measurements in the self-preserving jet. *Journal of Fluid Mechanics*, 38(3), 577-612.
[27] Phillips, O. M. (1955). The irrotational motion outside a free turbulent boundary. In Mathematical Proceedings of the Cambridge Philosophical Society (Vol. 51, No. 1, pp. 220-229). Cambridge University Press.
[28] Townsend, A. A. R. (1976). The structure of turbulent shear flow. Cambridge University Press.
[29] Stewart, R. W. (1956). Irrotational motion associated with free turbulent flows. *Journal of Fluid Mechanics*, 1(6), 593-606.
[30] Hinze, J. O. (1975). Turbulence, Second edition.
[31] Bisset, D. K., Hunt, J. C. R., Rogers, M. M., & Koen, D. (1999). Aspects of turbulent/non-turbulent interfaces.
[32] Bilger, R. W. (2004). Some aspects of scalar dissipation. *Flow, Turbulence and Combustion*, 72, 93-114.

ILA BERLIN 2024

PIONEERING AEROSPACE

For five days, between 5 and 9 June 2024, at Berlin/Brandenburg's airport BER, took place Innovation and Leadership in Aerospace fair – ILA Berlin. Taking as its slogan 'Pioneering Aerospace', the event gathered representatives of international industry, politics, the armed forces and science. Around 600 exhibitors from 31 countries presented a wide range of hi-tech and R&D projects.

COMOTI participated in this exhibition with its own stand, as part of the strategy to increase the visibility of the institute, to strengthen existing relations with partners in the field and to find new customers in these markets.

COMOTI`s participation in this event was a real success, making us visible to potential clients but also strengthening relations with our current collaborators and partners in the space and defence industry.

The main activity took place at COMOTI stand where we were visited by both commercial representatives who wanted to find new customers to sell products and services, as well as by our important customers and potential collaborators. We received the visit of many potential customers as well as existing partners from the space and defence industry, but also from Romanian officials, including a Romanian MoD delegation formed by Mr. Angel TÎLVĂR, Minister of the Ministry of National Defense, Lieutenant General Teodor INCICAȘ, Head of the General Directorate for Armaments and Major General Leonard BARABOI, Chief of Staff of the Air Force. We also had a meeting at the MTU Aero Engines AG booth, were we discussed, together with Mr. Wolfgang Gartner, ENGHE Program Director, the COMOTI's capabilities and also the contribution we can bring to the ENGHE project.

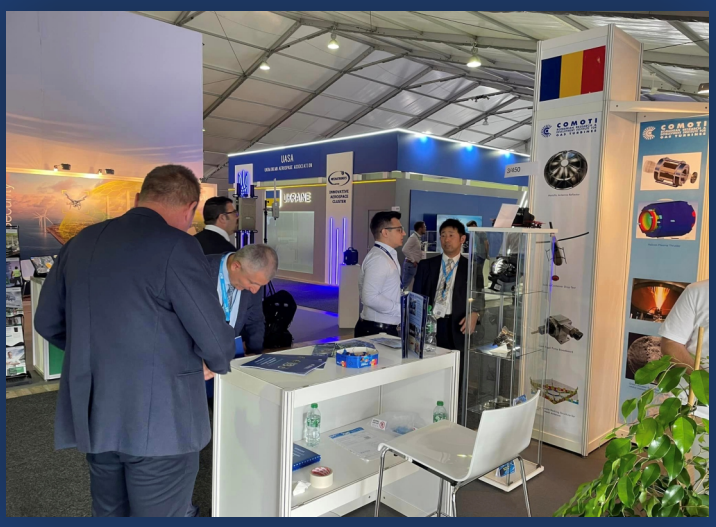

COMOTI

The only specialized company that integrates such activities as

scientific research,
design,
manufacturing,
testing,
experimental activities,
technologic transfer and innovation

in the field of aircraft and industrial gas turbines and high speed bladed machinery.

220D Iuliu Maniu Ave., 061206 Bucharest, ROMANIA,
P.O. 76, P.O.B. 174
Phone: (+4)021/434.01.98, (+4)021/434.02.31, (+4)021/434.02.40
Fax: (+4)021/434.02.41, e-mail: contact@comoti.ro

www.comoti.ro